Thesis for the degree of Licentiate of Philosophy

# Three-body cluster systems in the no-core shell model

Daniel Sääf


Department of Fundamental Physics
Chalmers University of Technology
Göteborg, Sweden 2014

Three-body cluster systems in the no-core shell model
Daniel Sääf



Department of Fundamental Physics
Chalmers University of Technology
SE-412 96 Göteborg
Sweden
Telephone +46 (0)31-772 1000

Cover:
Overlap function of $\left\langle {}^{6}\mathrm{He}(0^+)\right| {}^{4}\mathrm{He}(0^+) + n + n\rangle$ in the $S = L = 0$ channel. The two peaks correspond to the di-neutron and the cigar configurations, respectively, which are characteristic for Borromean two-neutron halo states. The microscopic derivation of the three-body overlap function and results will be presented further in Chap. 3.

Chalmers Reproservice
Göteborg, Sweden 2014

Three-body cluster systems in the no-core shell model

Daniel Sääf
Department of Fundamental Physics
Chalmers University of Technology

**Abstract**

In this thesis we present the *ab initio* no-core shell model (NCSM) and we use that framework to study $^6$He and $^6$Li computed with a realistic nucleon-nucleon interaction. In particular, we present results for the point-proton radius and the ground-state energy. Since we are limited to use a finite harmonic oscillator basis, we need to apply corrections to compute basis-independent results. A way of doing this is presented and demonstrated in this thesis. Furthermore, we derive an expression for calculating the three-body overlap function from microscopic wave functions obtained in the NCSM. We compute the overlap function, $\left\langle {}^6\mathrm{He}(0^+)\right| {}^4\mathrm{He}(0^+ + n + n\big\rangle$, to study the clusterization of the Borromean two-neutron halo state in $^6$He. We demonstrate that the clusterization is driven by the Pauli principle. The overlap function framework is also applied to $^6$Li. Finally, we demonstrate the capabilities of a microscopic model to study the core in a halo system, by computing the core swelling effect in $^6$He.

Keywords: no-core shell model, nuclear physics, halo nuclei, clusterization, core swelling

This thesis is based on work from the following two papers. In the main text these papers will be referred to as Paper 1 and Paper 2, respectively.

## Paper 1:

*Microscopic description of translationally invariant core + N + N overlap functions*
Daniel Sääf and Christian Forssén
Phys. Rev. C89 (2014) 011303(R), e-Print: arXiv:1309.5810

In this paper we derived an expression for computing the overlap function for a core+N+N system starting from microscopic wave functions obtained in the NCSM. In particular, we studied the two-neutron halo state in $^6$He, using realistic nucleon-nucleon interactions, by computing the overlap function $\langle {}^6\mathrm{He}(0^+) | \, {}^4\mathrm{He}(0^+ + n + n) \rangle$. By analysing the overlap functions we demonstrated that the clusterization is driven by the Pauli principle. We also computed the spectroscopic functions in a Hyperspherical Harmonic basis.

## Paper 2:

*Pushing the frontier of exact diagonalization for few and many-nucleon systems*
Boris D. Carlsson, Daniel Sääf, Håkan T. Johansson and Christian Forssén
Manuscritp in preparation

Here, we presented new developments of the exact diagonalization method as implemented in the NCSM. These developments allow us to diagonalize very large model spaces, with dimensions exceeding $10^{10}$. This gives us the opportunity to converge many-body systems computed with a bare chiral nucleon-nucleon interaction, in the NCSM. In particular, we presented results for $^6$Li in model spaces up to $N_{\max} = 22$ and $^{10}$B in model spaces up to $N_{\max} = 12$.

# Contents

# Chapter 1

# Introduction

This licentiate thesis presents the work studying the clusterization in light nuclei from microscopic wave functions. In particular, three-body structures will be studied and the example of $^6$He will be discussed. As an introduction to this specific aim we will in short terms explain the bigger picture in which this thesis should be seen.

In the quest of understanding matter, nuclear physics has played and is playing an important role. The standard model of particle physics today seems to cover the basic constituents of matter, such as quarks, leptons, force carriers and the Higgs boson, which recently was experimentally confirmed at CERN. As far as we know today, these particles are well described by quantum chromodynamics (QCD) and the electro-weak theory. When realizing this, a question arises: Do we completely understand what matter is and how it behaves starting only from its basic constituents? The answer to this question is very clearly no, otherwise the disciplines of nuclear and atomic physics would be completely useless. There are a couple of reasons why we are not able to use a reductionist view on matter and reduce matter to its basic building blocks. One of the reasons is that the normal matter, which we are surrounded by, is in a relative low-energy regime, which makes the quarks and the gluons condense and form color-neutral particles, hadrons. Color is the charge of the strong force that is described by QCD. There are a wealth of hadrons, the most important in nuclear physics are the nucleons: protons and neutrons, but also some of the mesons are important, in particular the lightest ones: pions. Protons and neutrons are bound together in atomic nuclei. Therefore, to understand the physics of the nucleus the energies related to quarks and gluons are not relevant, it exists a separation

of scales between the energy required to excite quarks and the energy regime needed to describe the low energy physics of the nucleus, such as the nuclear structure. Since the protons and neutrons are color neutral the force is a residual force, similar to the van der Waals force in chemistry. However, the force between the nucleons is related to the strong force described by QCD, but Another problem that makes it difficult to describe nuclei by the use of QCD is the many-body problem itself. Quantum mechanical problems are quite easy to solve if they are involving one or two bodies. The case of three bodies is a special case that may be exactly solvable, but when the number of degrees of freedom increases the complexity of the problem grows rapidly and a set of approximations are needed. The challenge of handling these problems is the task of nuclear physics.

Modern nuclear physics is a rich field covering many time- and energy scales and a lot of different physic. From the lightest isotopes with a few nucleons to nuclei consisting of hundreds of them. One topic that opens up the possibility to study the limits of the nuclear landscape is the study of nuclei close to the dripline. The dripline is the limit for bound nuclei. Nuclei close to the dripline are unstable and decay. Therefore, the development of modern radioactive beam facilities has been crucial to make it possible to create unstable nuclei and study them even if the decay time is short.

## 1.1 Halo physics

A particularly interesting type of many-body structure that appears close to the dripline is halo states. A halo nucleus can be effectively reduced from its many nucleonic degrees of freedom to a much simpler few-body system with a core and at least one valence nucleon loosely bound outside the core. A key feature of a halo state is the resulting large radius. A halo state can be formed when the barrier confining the nucleons is small. For this to happen the separation energy needs to be small and therefore the valence nucleons will be close to the continuum. These nucleons also need to be in a low angular momentum state, since the effective angular momentum barrier needs to be small. Even the Coulomb barrier needs to be low, which is the reason why neutron halo systems are more pronounced.

One characteristic property of a halo system is an enlarged radial extension [1]. It was through extracting the root-mean-square (rms) matter radius from interaction cross-section measurements that Tanihata et al. [2]

discovered the first nuclear halo state in $^{11}$Li.

The ground states of $^{11}$Li and $^{6}$He are examples of two-neutron halo nuclei, with two neutrons and a core. A property that makes these three-body states particularly interesting is that the subsystems are unbound. The two-body subsystems of $^{6}$He are $^{5}$He and 2n, which both are unbound. This is the reason why these systems usually are called Borromean three-body halo systems [3]. The name Borromean originates from the Borromean rings, which is a system of three rings connected to each other, in such a way that if one ring is removed the two other rings are unconnected.

## 1.2 *Ab-initio* methods

If the use of radioactive beam facilities has created the possibility to experimentally study exotic structures, recent developments in theoretical nuclear physics have opened up the possibility to understand why these exotic structures exist and in detail try to understand the nuclear force. These developments are usually grouped under the label *ab initio* methods. *Ab initio* is a Latin term meaning 'from the beginning'. In nuclear physics it is used to describe a method that starts from the most basic principles governing the nucleus and computes observables in a systematic way. The aim is to control all approximations done in the calculation and therefore the ambition is to present all results with both systematic and statistical uncertainties. In this way *ab initio* methods creates the possibility to connect the underlying theory to observables. It also makes it possible to compute observables that are not to experimentally feasible to measure, but still can be important. An example where this kind of data can be important is in the understanding of the nucleosynthesis.

Another reason for the progress of *ab initio* methods, is the increase of computational power. The *ab initio* approach results in large-scale problems that need modern highly parallel and efficient computational resources.

Another reason behind the advance of *ab initio* methods is the development of realistic nuclear interactions. This is an ongoing work, where the chiral effective field theory (EFT) approach seems to be the most suited. The nuclear structure obtained in this work is obtained with potentials derived from chiral EFT.

A final important reason is that the theory of many-body methods has developed, and today there are a number of efficient many-body models that

can be benchmarked against each other and that can be used with different purposes.

This introduction sets the stage for this thesis, where we will present our first-principle studies of the clusterization of $^6$He, which is the lightest Borromean two-neutron halo nucleus. The outline of this thesis is the following: In Chap. 2 the no-core shell model (NCSM), which is the *ab initio* model used in this work will be described and computed results for the ground state energy and radius for $^6$Li and $^6$He will be presented. In Chap. 3, a formalism for studying the clusterization in NCSM will be presented and some results will be shown. In Chap. 4, we will focus on the core and present an ongoing work studying core swelling. Finally, the thesis ends with a conclusion of this work and an outlook of the continuation of this research.

# Chapter 2

# No-Core Shell Model

To be able to solve the $A$-body Schrödinger equation, a many-body method needs to be used. In this work, with a focus on the light nuclei and in particular $^6$He, NCSM has been the method of choice. I will, in this chapter give a brief description of the model and explain why it is suitable for our purposes.

The name of NCSM suggests a similarity with the nuclear shell model. However, the most important difference is that the NCSM treats all particles as active, hence no-core in the name. The idea is to use the harmonic oscillator (HO) basis and powerful second-quantization techniques, but with realistic nucleon-nucleon interactions and with the aim to solve the full A-body problem without approximations. The interactions used in this work will be further discussed in Sec. 2.3.

The specific aim is to solve the A-body Schrödinger equation

$$H_A\psi_A = E_A\psi_A, \tag{2.1}$$

which is the equation governing a non-relativistic quantum system. This goal is achieved by expressing the Hamiltonian in a many-body basis and diagonalizing the resulting matrix to get the eigenvalues $E_A$ and the eigenvectors $\psi_A$. The dimension of the matrix is huge because it grows with A and the eigenvalue problem converges slowly. A diagonalization method with the capability to handle this kind of problems is the Lanzcos method, which is used in most of the present-day NCSM calculations and in all calculations presented in this thesis. The Lanzcos algorithm is an iterative method and doesn't compute the full spectrum of eigenstate. For further details of the Lanzcos algorithm see Ref. [4, 5].

## 2.1 Many-body theory and second quantization

A fundamental tool that is used in NCSM and is utilized extensively in this thesis is the second quantization formalism. This framework is based on the concept of creation and annihilation operators and Fock space. A fermionic single-particle (sp) state is denoted $|\alpha\rangle$, where $\alpha$ is a set of quantum numbers needed to describe the state. In second quantization it is possible to write the same state as a fermionic creation operator acting on the vacuum,

$$a_\alpha^\dagger |0\rangle = |\alpha\rangle \,.$$

We can also introduce an annihilation operator, $a_\alpha$, which annihilates the state $|\alpha\rangle$. The annihilation operator is the Hermitian conjugate of the creation operator.

The Fermi-Dirac statistic of fermions are ensured by the anticommutation rules for the creation and annihiliation operators. The anticommutation rules for fermions are

$$\{a_\alpha^\dagger, a_\beta^\dagger\} = 0 \qquad \{a_\alpha, a_\beta\} = 0 \qquad \{a_\alpha^\dagger, a_\beta\} = \delta_{\alpha,\beta}. \tag{2.2}$$

In this framework it is now possible to create antisymmetric many-body states, named Slater determinant (SD) states, by acting with multiple creation operators in a given order,

$$a_{\alpha_A}^\dagger a_{\alpha_{A-1}}^\dagger \dots a_{\alpha_1}^\dagger |0\rangle = |\alpha_1, \dots \alpha_{A-1}\alpha_A\rangle \,. \tag{2.3}$$

The basis employed in NCSM computations needs to treat both protons and neutrons. This can be achived by using the isospin formalism, which adds two quantum numbers to describe the state: the isospin $t$ and its projection $m_t$. For nucleons we have $t = \frac{1}{2}$ and $m_t = \frac{1}{2}$ for proton states ($m_t = -\frac{1}{2}$ for neutron states). Many-body theory and second quantization is a broad subject, that can be studied in more details in for example [6, 7]

## 2.2 Many-body basis

The many-body basis consists of A-body SD states, as introduced in Sec. 2.1. The most important feature of the SD states is that they are completely

antisymmetric with respect to particle exchange. Every SD state is composed of a linear combination of $A$ sp states in absolute coordinates. In the NCSM, these sp states correspond to HO states. The HO sp states are in coordinate representation defined as:

$$\begin{aligned}\psi_{nlj}(\vec{r},\sigma:b) &= \langle r,\hat{r},\sigma:b|\ nljm\rangle \\ &= R_{nl}(r:b)\left[Y_l(\hat{r})\times\xi_{\frac{1}{2}}\right]^j_m\end{aligned} \tag{2.4}$$

where the spin, $s=\frac{1}{2}$, is coupled together with the orbital angular momentum $l$ to a total spin $j$, with a $z-$projection $m$. $\sigma$ is the spin coordinate and $b$ is the HO length and is related to the HO frequency, $\Omega$, via

$$b=\sqrt{\frac{\hbar}{m\Omega}}. \tag{2.5}$$

The HO frequency is a basis parameter that can be varied together with the basis truncation (see below). The quantum number $n$ is the principal quantum number and corresponds to the number of radial nodes of the HO function. The combination $N=2n+l$ is called the major HO shell number.

The HO basis has certain advantages that makes it useful in many-body calculations. First of all, the HO basis states are easy to handle both in momentum and in position space. This makes it possible to compute matrix elements from interactions expressed both in position and momentum space.

Another advantage is that there are algebraic transformations that simplify the calculations. For example, the Talmi-Moshinsky transformation makes it possible to transform a system of two HO states described with absolute coordinates to a system described in relative coordinates [8]. This will be important in the derivation of the overlap functions described in Chap. 3.

Finally, a very prominent advantage with a HO basis is that it is possible to select a truncation so that an $A$-body state can be defactorized into one part dependent only on the center of mass (CM) motion and one part dependent on the intrinsic motion, even if sp coordinates are used. The trick is to truncate the many-body basis by a maximum total HO energy. The physical eigenstate, which is translationally invariant, can be selected by shifting all spurious CM excitations up in the eigenspectrum using a Lawson projection term [9]. The obtained eigenstates in the SD basis can then be written as

$$\begin{aligned}&\langle\vec{r}_1\ldots\vec{r}_A\sigma_1\ldots\sigma_A\tau_1\ldots\tau_A|\ AJM\rangle_{SD} \\ &=\left\langle\vec{\xi}_1\ldots\vec{\xi}_A\sigma_1\ldots\sigma_A\tau_1\ldots\tau_A\right|\ AJM\Big\rangle\,\Psi_{000}(\vec{\xi}_0),\end{aligned} \tag{2.6}$$

where $\xi_i$ are relative Jacobi coordinates and the CM motion is in the $0S$ ground state. In principle, a complete many-body basis will assure that the Schrödinger equation is solved exactly. In practice, however, the basis needs to be truncated. The truncation scheme that we use is consequently based on the total energy of the many-body state. The total energy of a SD state is the sum of the energies of the $A$ HO states,

$$E_{\rm tot} = \sum_{i=1}^{A} N_i \hbar\Omega = \sum_i (2n_i + l_i)\hbar\Omega = N_{\rm tot}\hbar\Omega.$$

Instead of labelling a many-body truncation by $\max(\sum_i N_i) \leq N_{\rm tot}$ we rather introduce the parameter $N_{\rm max}$, which measures the maximal allowed number of HO excitations above the lowest possible configuration. For s-shell nuclei $N_{\rm max} = N_{\rm tot}$, but for p-shell nuclei it will depend on how many particles are in the $N = 1$ shell in the lowest configuration. For example, in $^6$Li $N_{\rm max} = N_{\rm tot} - 2$. In Fig. 2.1 we illustrate four different configurations of $^6$Li.

There is a choice in how we can treat the spin of the many-body states. Either the sp states in a many-body state can be spin-coupled to a total $J$, which then is a good quantum number of the basis. This is called the J-scheme. The other option is that the sp states can be uncoupled with $M_J$ as a good quantum number. We are using this scheme, which is called the M-scheme. In this scheme $M_J = \sum_{i=1}^{A} m_i$. In addition, parity $\pi$ and $M_T$ are also good quantum numbers. The advantage of the m-scheme is that the antisymmetrization is trivially achieved by the SD basis and there is no need to include spin-coupling algebra. The disadvantage is that the many-body basis becomes much larger compared with the J-scheme. For systems with more then four nucleons the m-scheme is more efficient and it is therefore used in most NCSM calculations.

## 2.3 Realistic nuclear interaction

A specific goal of *ab initio* nuclear structure calculations is to employ and test realistic nuclear interactions. Our fundamental understanding of the nuclear interaction is based on QCD, which is the theory explaining the strong interaction between quarks and gluons. Nuclear structure is a low-energy phenomenon on the scale of subatomic physics and since QCD is

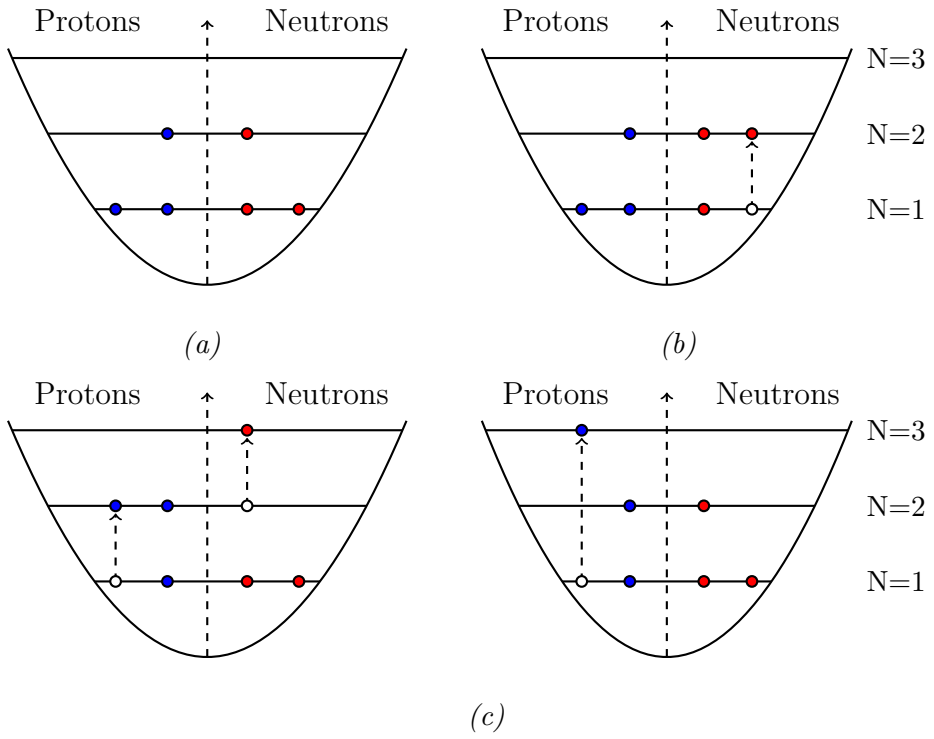


*Figure 2.1: Sketch of many-body states in $^6Li$. Panel a: $N_{\max} = 0$ configuration. Panel b: $N_{\max} = 1$ configuration. Panel c: $N_{\max} = 2$ configurations. All $N\hbar\Omega$ configurations with $N \leq N_{\max}$ span the $N_{max}\hbar\Omega$-space.*

non-perturbative in this low-energy regime it is very difficult to use it in direct computations. One way of overcoming this issue is to apply the concept of an effective field theory (EFT). The crucial point in an EFT is to identify a separation of scales. In the case of low-energy nuclear physics a natural separation of scales can be observed based on that $m_\pi \ll m_\rho$, which corresponds to that the appropriate degrees of freedom are nucleons and pions. To understand nuclear structure in a low-energy limit quarks and gluons are not needed explicitly, neither are excitations of the nucleons and the mesons heavier then the pions. Based on this it is now possible to write down all Feynman diagrams allowed by the symmetries of the underlying theory, QCD. The Feynman diagrams are ordered in powers of $(m_\pi/m_\rho)$, where the leading order (LO) is the most important one. The EFT needs to be renormalized and therefore a chiral regulator, $\Lambda_{EFT}$ is needed.

The effect of using an EFT in a low-energy regime is that all short-range physics from QCD are condensed into contact terms in the Feynman diagrams. These contact terms can be determined by fitting experimental nucleon-nucleon scattering data. In this work two different potentials based on chiral EFT have been used. The first one was developed by Entem and Machleidt [10] and contains diagrams up to next-to-next-to-next-to leading order (N3LO). This potential will further on be referred to as Idaho-N3LO (I-N3LO). The other one, NNLOopt, was developed by Ekström et al. [11] including diagrams up to NNLO. The low-energy constants in the NNLOopt potential was determined by using a modern mathematical optimization algorithm, POUNDERS [12]. Both NNLOopt and I-N3LO use a chiral regulator with $\Lambda_{EFT} = 500$ MeV. Results from computations with I-N3LO and NNLOopt will be presented in Sec. 2.6.

### 2.3.1 Three-body forces

For a complete description of nuclear forces it is not enough with a nucleon-nucleon (NN) interaction. A realistic interaction-model therefore needs to include also irreducible many-body forces. In the chiral EFT power counting the three-body force diagrams enter at next-to-next-to-leading order (NNLO) but still seem to play an important role in reproducing the physics of atomic nuclei. In this work we have only considered two-body forces because it gives us the opportunity to solve the eigenvalue problem in really large model spaces. Furthermore, the derivations of overlap functions presented in Chap. 3 are not restricted to any specific type of interaction.

### 2.3.2 Unitary transformations

Realistic nucleon-nucleon potentials are characterized by a hard core (short-range repulsion) and a strong tensor force. The result of this is that low-energy physics is still dependent on higher momentum modes, and that very large model spaces are required to capture all UV physics. There are different solutions to this problem, but a particular useful one is to apply a unitary transformation that uncouples the low- and high-momentum modes from each other while keeping the observables unchanged. This procedure can be viewed as lowering the resolution scale of the problem to one that is more suitable to use. The transformation needs to be unitary to keep the

observables, such as the energy, invariant. The unitary transformation used in this work is the similarity renormalization group (SRG) [13].

The SRG transformation is implemented as a flow equation and uses a diagonal flow-generator to suppress the off-diagonal matrix elements in momentum space. The transformation will therefore evolve the potential towards a band-diagonal form and decouple the high-momentum modes. There is a flow parameter, $\Lambda_{\mathrm{SRG}}$, which is defined such that $\Lambda_{\mathrm{SRG}} = \infty$ means no transformation and $\Lambda_{\mathrm{SRG}} = 0$ corresponds to taking the flow to infinity. One of the properties of SRG is that it induces many-body forces. The calculations performed in the scope of this work will only take into account two-body forces. This approximation violates the unitarity of the transformation and creates a small dependence on the SRG flow parameter. The magnitude of this dependence can be seen as an indicator of missing induced many-body forces. This will be seen in the results presented in Sec. 2.6.

## 2.4 Infrared and ultraviolet cutoff

The truncation of the many-body basis introduces a dependence on the basis parameters $N_{\mathrm{max}}$ and $\hbar\Omega$. In the limit of infinite model space, this dependence will vanish. But for finite spaces there will be a correction to the obtained result. One way of correcting for the finite space is to translate the basis parameters to quantities that correspond more directly to the physics of the many-body problem. The natural parameters are based on the momentum-scale limitations of the HO basis. It is possible to define two cutoffs corresponding to the maximal momentum, $\lambda_{\mathrm{UV}}$ and a maximal length, $L$. With these parameters it is possible to understand the corrections from a physical point of view and to use this understanding to extrapolate to an infinite basis.

It has been shown that a truncation of the oscillator basis can be viewed as solving the Schrödinger equation in a sphere with a Dirichlet boundary condition at the radius $L$ [14]. This radius, that roughly corresponds to the radial extent of the HO basis, is effectively an infrared cutoff. The naive estimate of $L$ is the maximum displacement of a particle in a HO with the maximum energy included in the basis. This displacement is also known as the classical turning point. The energy of a HO single-particle state is

$E = (N + \frac{3}{2})\hbar\Omega$. The maximum displacement is therefore [14]

$$L_0 = \sqrt{2(N + \frac{3}{2})}b,$$

where $b$ is defined in Eq (2.5).

In two-body systems one can show that the naive estimate is not a very good approximation for the infrared cutoff. Instead, More et al. [15] suggested, based on empirical studies and an analytical derivation, that the infrared cutoff should be defined as

$$L_2 = \sqrt{2(N + \frac{3}{2} + 2)}b. \tag{2.7}$$

The analytical derivation is based on a semi-classical approach for the two-body system, and by computing the smallest eigenvalue of the squared momentum operator, $\kappa_{\min}$, in a HO basis and comparing with the lowest eigenvalue of the squared momentum in a spherical box. The extrapolations presented in Sec. 2.6 will use $L = L_2$. When applying this approach to a many-body basis it is possible that the IR cutoff is not correctly described by $L_2$. In this work $L_2$ will be used as an approximation of the IR cutoff also in many-body systems, and there are results presented in Sec. 2.6 that may indicate problems with this choice that needs to be studied further.

The maximal momentum that can be captured in a HO basis is

$$\Lambda_{UV} = \sqrt{2(N + \frac{3}{2})}\hbar/b, \tag{2.8}$$

as obtained from the highest single-particle state in the basis [14]. This momentum will be used as an ultraviolet (UV) cutoff. It is important to note that the interaction based on chiral EFT already has a momentum cutoff from the chiral regulator. This leads to the possibility that when the $\Lambda_{UV}$ is well above $\Lambda_{EFT}$, all UV physics included in the interaction should be captured by the many-body basis and there is no need for an UV correction. The computed results will then be considered as UV converged. The reason why it is not enough to have that $\Lambda_{UV} = \Lambda_{EFT}$ is that the chiral regulator is not a sharp cutoff, it just suppresses momenta above $\Lambda_{EFT}$ exponentially [16]. Therefore, the HO basis needs to have a higher UV cutoff than the chiral regulator.

## 2.5 Corrections due to the infrared cutoff

When calculations are performed with an UV cutoff high sufficient to capture all UV physics included in the interaction, i.e. UV converged, it is enough to focus on the IR truncation and try to understand how the IR correction influences the observable and how it is possible to extrapolate to an infinite cutoff. The corrections due to the infrared cutoff have been derived for both energy and radius [14, 15]. The basic idea behind these derivations is to analytically compute the difference between solving the single-particle Schrödinger equation in a box with Dirchlet boundary conditions at $L$, and solving the equation without the box. In [14, 16] a leading-order correction is derived, which for the energy is

$$E(L) = E_\infty + A_\infty e^{(-2k_\infty L)} + \mathcal{O}(e^{(-4k_\infty L)}), \tag{2.9}$$

where $k_\infty$ is related to the single-nucleon separation energy of the nucleus. However, in practice we will treat all three parameters $A_\infty$, $k_\infty$ and $E_\infty$ as fitting parameters.

Furthermore, Furnstahl et al. [14] suggest an expression for the correction of the squared radius as a function of the infrared cutoff

$$< r^2 > \approx < r^2 >_\infty [1 - (c_0\beta^3 + c_1\beta)e^{-\beta}], \tag{2.10}$$

where $\beta = 2k_\infty L$. In this work $c_0, c_1$ and $< r^2 >_\infty$ are treated as fit parameters, while $k_\infty$ is fixed from the energy fit.

By applying this theory it is possible in principle to extract a result independent on the basis used. It is also possible to extract a statistical error due to the curve fit. This error will be presented together with the extrapolated result. However, it is important to note that there might be systematical errors larger than the statistical ones that still needs to be studied.

## 2.6 Results

In this work we have focused on applying our formalism to light nuclei with $A = 6$. The main focus in this thesis is $^6$He, but also some results for $^6$Li will be presented. The observables we have have mostly studied are the energy and the radius of the ground state.

### 2.6.1 Binding energy of $^6$He and $^6$Li

In Fig. 2.2 the results for the ground state of $^6$He is presented as a function of the HO frequency. What is noticeable is that when the size of the model space increases the results become less dependent on the HO frequency, which is what is expected according to the theory presented in Sec. 2, since in the infinite model space the results shall be basis independent. Another characteristic property is how the results are following the variational principle, since the ground state energy converges from above. This is also a characteristic and useful property of NCSM.

The same data as showed in Fig. 2.2 can be represented as functions of the UV and IR cutoffs. From this representation we can attempt of extract a model-independent, extrapolated results. This is done by transforming the parameters, $N_{\max}$ and $\hbar\Omega$, to the UV cutoff, $\Lambda_{UV}$, and the IR cutoff, $L_2$, defined in Sec. 2.4 and applying the correction formula (2.9). In this extrapolation all data points with $\Lambda_{UV} > 700$ MeV are included. The reason is to assure that UV convergence is reached, which is visible in the extrapolation pattern. The chiral regulator of the I-N3LO interaction is $\Lambda_{EFT} = 500$ MeV and the SRG transformation pushes down the high-momentum physics even lower, which makes $\Lambda_{UV} > 700$ MeV a reasonable cutoff to assure UV convergence. In the right-most part of the figure the extrapolated results are shown, including statistical error bars from the curve fit. Three extrapolations are performed, each one includes data points up to a certain $N_{\max}$. The first one includes points up to $N_{\max} = 12$, the second up to $N_{\max} = 14$ and the final one includes all data points ($N_{\max} \leq 16$). This sequence is created to test the stability of this procedure and it shows that the extrapolation seems to be quite robust in this sense, which opens up the possibility to use this extrapolation scheme in cases where it is difficult to compute IR converged results. In the case presented here, even a set of $N_{\max} = 12$ calculations would have given a good hint of the final result. One of the reasons for this can be observed in Fig. 2.4 where all data points included in the extrapolation done in Fig. 2.3 are marked with a red diamond. What can be seen here is that data points computed in small model spaces, but with a high frequency resulting in a high UV and low IR cutoffs, are included in the fit and aligns quite good in the slope.

Some of the results published in Paper 1 are presented in Table 2.1. The table shows the computed ground state energy for $^6$He and the two neutron separation energy which is one of the characteristic properties for the halo-

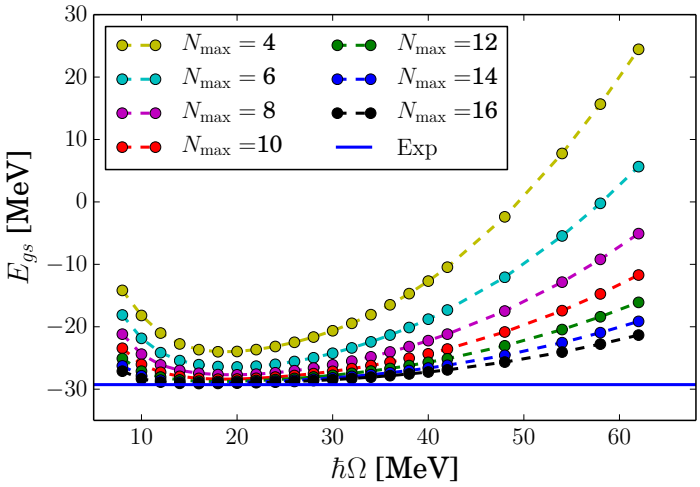


*Figure 2.2: Ground state energy of $^6$He computed with the SRG-evolved I-N3LO interaction ($\Lambda_{\mathrm{SRG}} = 2.0$ $fm^{-1}$).*

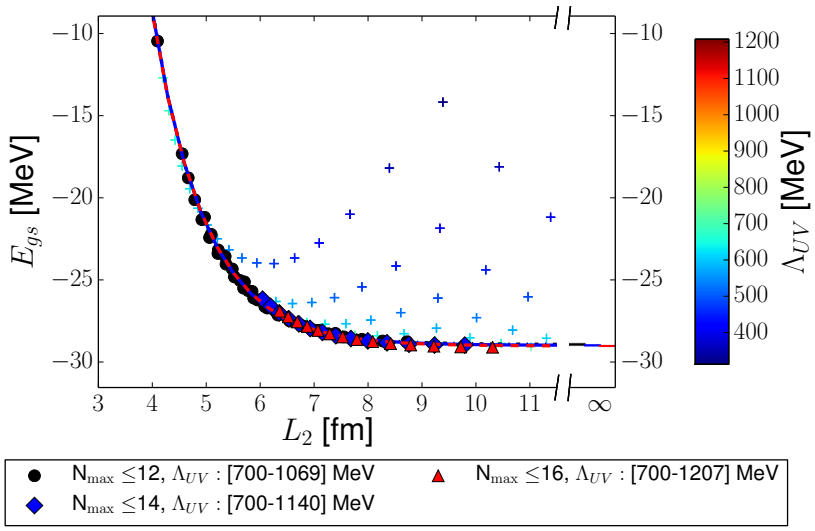


*Figure 2.3: Ground state energy of $^6$He with I-N3LO and $\Lambda_{\mathrm{SRG}} = 2.0$ $fm^{-1}$. The extrapolation includes all data points with $\lambda_{UV} > 700$ MeV. The error bars presented in the right part of the figure only correspond to the statistical error from the fit.*

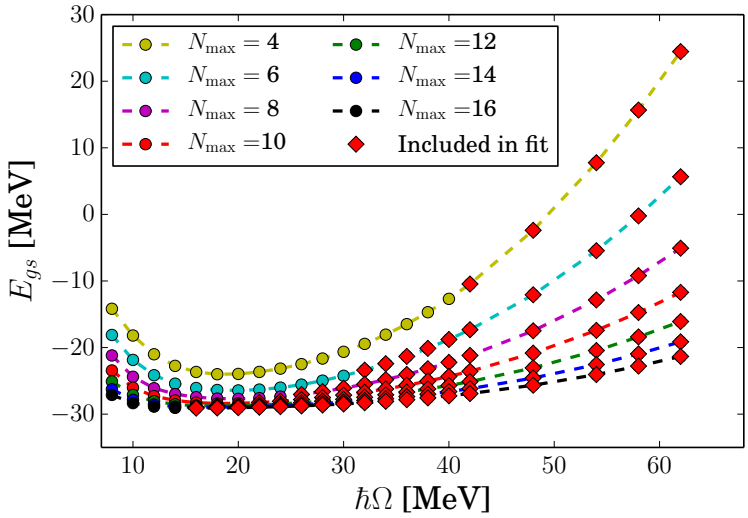


*Figure 2.4: Same data as used in Fig. 2.2. However, the data points that are actually used in the fit presented in Fig. 2.3 are marked with a diamond.*

structure of $^6$He. The dependence on $\Lambda_{\mathrm{SRG}}$ is noticeable both for the ground state energy and the separation energy and is due to the violation of the unitarity when only including induced two-body forces.

To show the UV convergence more clearly, in Fig. 2.5 data points with fixed $\Lambda_{UV}$ have been used for the extrapolation and what can be seen is that the $\Lambda_{UV}$-dependence decreases when $\Lambda_{UV}$ increases. Above $\Lambda_{UV} = 800$ MeV the results seem to be UV converged. Note that these results are obtained with the NNLOopt interaction, therefore it is not comparable with the $\Lambda_{UV}$ cutoff used in Fig. 2.3.

Recent code developments [20], together with access to dedicated computer resources have increased our capabilities to obtain results in large model spaces. The code developments are presented in Paper 2, together with numerical results. The largest model space that we have performed calculations for is $^6$Li, at $N_{\max} = 22$, which includes $2.5 \times 10^{10}$ many-body states. In Fig. 2.6 the results and the extrapolation is displayed and note that we can basically reach numerical convergence for a bare realistic interaction in an $A = 6$ system. However, it is also clear that there is a problem with the extrapolation. The extrapolated result is above the lowest lying data points, which cannot be correct since the results must obey the variational principle. This

*Table 2.1: Extrapolated results for the ground state energy, two-neutron separation energy and point-proton radius in $^6$He. Computed with SRG-evolved I-N3LO. The extrapolation includes data points with $N_{\max} \leq 16$. The results by Bacca et al. results are obtained using the Hyperspherical Harmonics Method with I-N3LO interaction evolved with $V_{\mathrm{low}-k}$.*

| | Exp. [17] | This work | | | Bacca *et al.* [18, 19] |
|---|---|---|---|---|---|
| | | $\Lambda_{\mathrm{SRG}} = 1.8$ | $\Lambda_{\mathrm{SRG}} = 2.0$ | $\Lambda_{\mathrm{SRG}} = 2.2$ | $\Lambda = 2.0$ fm$^{-1}$ |
| $E_{\mathrm{gs}}$ [MeV] | 29.269 | 29.67(3) | 29.20(11) | 28.61(22) | 29.47(3) |
| $S_{2n}$ [MeV] | 0.975 | 1.22(2) | 0.95(10) | 0.68(22) | 0.82(4) |
| $r_{\mathrm{pt-p}}$ [fm] | 1.938(23) | 1.820(4) | 1.820(4) | 1.815(8) | 1.804(9) |

*Table 2.2: Extrapolated results for the $^6$Li ground state computed with NNLOopt and model spaces with $N_{\max} \leq 22$ and $\Lambda_{UV} > 880$ MeV.*

| | Exp.[21] | This work NNLOopt |
|---|---|---|
| $E_{\mathrm{gs}}$ [MeV] | 31.99 | 30.30(10) |

disagreement may be due to a wrong choice of the infrared cutoff. The results for $N_{\max} = 22$ with the NNLOopt interaction is presented in Table 2.2.

### 2.6.2 Radius of $^6$He and $^6$Li

To study the size of atomic nuclei we are limited to compute the point-proton or the point-neutron radii since the NCSM treats the nucleons as point-particles. To be able to compare the computed results with experimental data the charge-radius needs to be extracted from the point-proton radius. The relation between the point-proton radius, $r_{pt-p}$ and the charge radius, $r_{ch}$ can be written [22]

$$r_{pt-p}^2 = r_{ch}^2 - R_p^2 - (N/Z)R_N^2 - 3/(4M_p^2) - r_{SO}^2, \tag{2.11}$$

where $R_p$ and $R_n$ is the radius of the proton and neutron, respectively. The term $3/(4M_p^2)$ is the first-order relativistic correction term and $r_{SO}^2$ is the spin-orbit correction. In the following section only the point-proton radius will be presented and the experimental data will be translated to this measure.

In Fig. 2.7 the point-proton radius for $^6$He is presented as a function of HO frequency. When analysing a similar figure for the energy of the ground

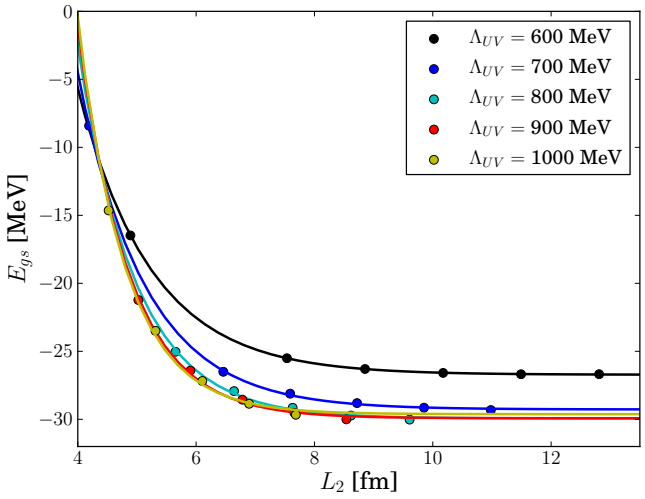


*Figure 2.5: Ground state energy for $^6$Li computed with the NNLOopt interaction for series of fixed $\Lambda_{UV}$. Figure shows the dependence on the UV cutoff. Model spaces with $N_{\max} \in [6, 16]$ are included in the fit.*

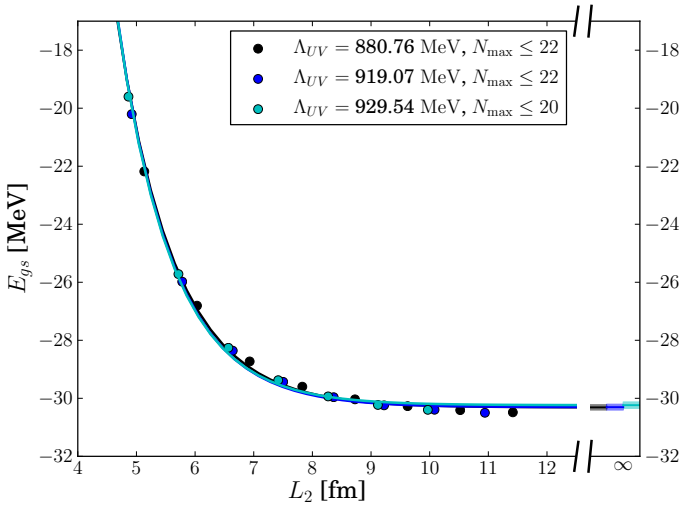


*Figure 2.6: Ground state energy for $^6$Li computed with the NNLOopt interaction. The data points included in the fit are well UV converge and the figure shows the IR convergence. In the right part of the figure the extrapolated result with the statistical error from the curve fit is presented.*

state of $^6$He (Fig. 2.2) the variational principle was used as a guideline to extract an energy. In this case there is no obvious way to extract a value for the point-proton radius.

However, we can also for this case introduce the UV and IR cutoffs. The results are displayed in Fig. 2.8, where Eq. (2.10) is used to correct for the finite basis. What is observed in Fig. 2.8 is that the data points align quite well with the extrapolation and we are able to extract a result with a statistical error corresponding to the curve fit. The statistical errors are displayed as error bars in the right-part of the figure. By comparing the three extrapolations performed for different $N_{\max}$ the results may indicate that there are systematical errors larger than the statistical ones. This may be due to that $L_2$ does not correspond to the correct IR cutoff. Extrapolated radii results for $^6$He are presented in Table 2.1.

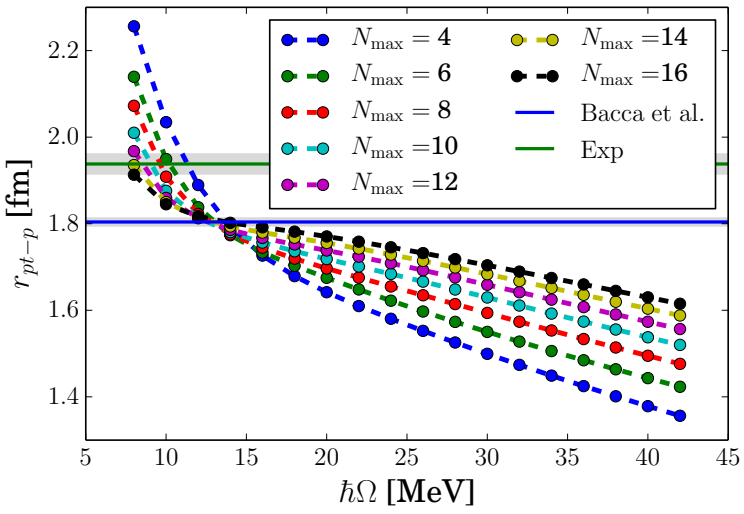


*Figure 2.7: Point-proton radius of $^6$He computed with the SRG-evolved I-N3LO interaction ($\Lambda_{\mathrm{SRG}} = 2.0\ fm^{-1}$). Resutls by Bacca et at. [18, 19] are obtained with the Hyperspherical Harmonic Method.*

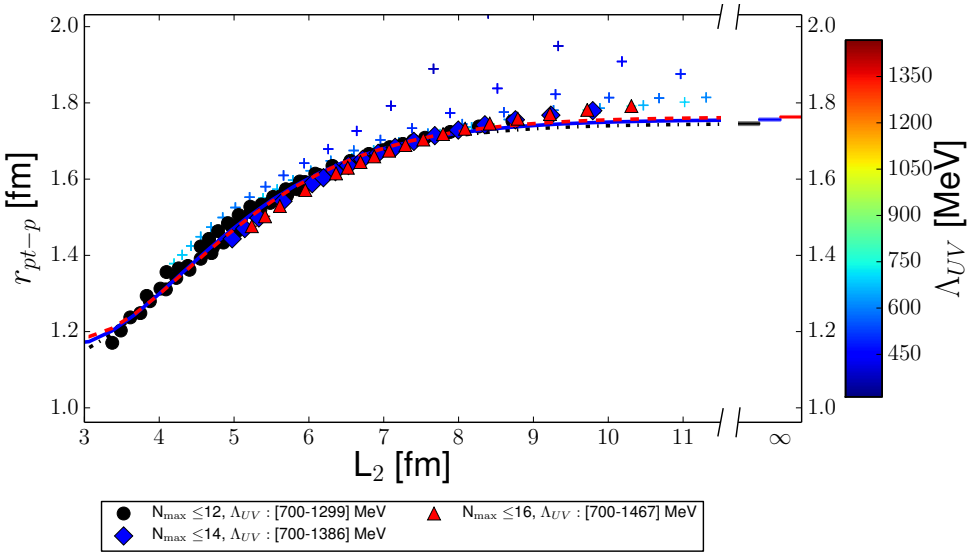


*Figure 2.8: Point-proton radius of $^6$He computed with a SRG-evolved I-N3LO interaction ($\Lambda_{\mathrm{SRG}} = 2.0\ fm^{-1}$).*

# Chapter 3

# Three-body cluster system

The ability to compute translationally invariant wave functions in NCSM opens up the possibility to study in detail the structure of the nucleus. When approaching the nuclear dripline a landscape of cluster structures emerges that is interesting to study from an *ab initio* perspective. A particular type of cluster structure that has been studied in the past is the Borromean three-body core+n+n found in, for example, halo states of $^6$He and $^{11}$Li. In Sec. 1.1 a general introduction to $^6$He and the characteristic properties of a Borromean halo was presented. A part of this work has been to study the clusterization of $^6$He from a microscopic perspective by calculating translationally invariant cluster form factors for the Core+N+N channel. This allows us to study $^6$He as a three-body system consisting of a $^4$He-core and two neutrons.

In the following chapter the theory behind Paper 1 will be explained in further detail and additional results will be presented.

## 3.1 Overlap function

To introduce overlap functions in general terms, we can start with the definition of the two-body overlap function. It is defined to be the integral over three wave functions, $\psi_A^{J_A M_A}$, $\psi_B^{J_B M_B}$ and $\psi_C^{J_C M_C}$, where $A, B$ and $C$ are the numbers of nucleons in each nuclei. The nucleus $A$ consists of the nucleons from $B$ and $C$, $A = B + C$. The $J_i$ and $M_i$ are the spin and the projection quantum number, respectively. The integral is over the internal coordinates of the wave functions $B$ and $C$, which results in that the overlap function is

a function of the relative coordinate $r$, between the wave functions $B$ and $C$. The general definition of the two-body overlap function is

$$u^{J_A M_A}_{J_B M_B, J_C M_C}(\vec{r}) = \int d\vec{x} d\vec{y}\ \psi_A^{J_A M_A}(\vec{r}, \vec{x}, \vec{y}) \psi_B^{J_B M_B *}(\vec{x}) \psi_C^{J_C M_C *}(\vec{y})$$

Another important quantity to introduce is the spectroscopic factor, which is the norm of the squared overlap function. An important thing to note is that the overlap function as well as spectroscopic factor are non-observables. A non-observable is a property that is model dependent. The non-observables that we are going to consider takes the form of a matrix element of an operator, $O$. We are free to apply a unitary transformations $U$ to the operator, $O$ and states $|\psi_m\rangle$.

$$O_{mn} = \langle \psi_m | O | \psi_n \rangle = (\langle \psi_m | U^\dagger) U O U^\dagger (U | \psi_n \rangle) = \left\langle \widetilde{\psi}_m \middle| \widetilde{O} \middle| \widetilde{\psi}_n \right\rangle$$

This results in that the matrix elements are invariant, although the operator itself, between the transformed states, is in general changed,

$$\widetilde{O}_{mn} = \left\langle \widetilde{\psi}_m \middle| O \middle| \widetilde{\psi}_n \right\rangle \neq O_{mn}.$$

In the low-energy limit we are working in, an example of a unitary transformation that can be applied is a transformation that modifies short-range unresolved physics, which will not modify observables such as the energy. Therefore, we do not have a set of preferred states and our non-observables will be dependent of how we choose our Hamiltonian. The interpretation of non-observables are discussed in further details in Ref. [23].

Another important quantity is the spectroscopic factor, which is the norm of the squared overlap function. The spectroscopic factor is also a non-observable.

The two-body overlap function has already been studied in the NCSM [24], and expressions for translational invariant form factors were derived. In order to introduce the formalism we will start with the simplest case found in Ref. [24], which is the Core+N overlap function that is obtained from the overlap integral

$$u^{A\lambda JT}_{(A-1)I_1T_1, I_2T_2}(\eta) = \langle A\lambda JT | \mathcal{A}_{A-1,1} \Phi^{A\lambda JT}_{(A-1)\lambda_1 I_1 T_1, I_2 T_2}; \delta_\eta \rangle. \tag{3.1}$$

The bra in this expression corresponds to an $A$-nucleon state with total spin (isospin) J (T) and an additional quantum number $\lambda$ needed to characterize

the eigenstate. The ket corresponds to a two-body cluster state consisting of an $(A-1)$-nucleon state with quantum numbers $I_1T_1$, and a single-nucleon state with $I_2T_2$ as quantum numbers. We will keep this general notation although it is clear that $I_2 = T_2 = \frac{1}{2}$ in this case. The large cluster will be described in a SD basis and while the small one, which in this case consists of a single nucleon, will be expressed in relative coordinates. The distance between the two clusters is described by the normalized Jacobi coordinate,

$$\vec{\eta} = \sqrt{\frac{(A-a)a}{A}}\left[\frac{1}{A-a}\sum_{i=1}^{A-a}\vec{r}_i - \frac{1}{a}(\vec{r}_{A-a+1} + \vec{r}_A)\right],$$

shown in Fig.3.1 (a). This definition is for the general case where the small cluster consist of $a$ nucleons, in this case $a = 1$. The distance between the clusters is represented in a complete basis of the continuous coordinate $\eta$, where every basis function corresponds to a frozen relative distance. This is reflected in the Dirac $\delta$ function. Furthermore, $\mathcal{A}_{A-1,1}$ is a cluster antisymmetrizer that ensures antisymmetrization with respect to exchange of nucleons between the clusters.

To generalize the overlap function to three-body systems, we will consider a large cluster with $A-a$ nucleons and two small clusters with $a_2$ and $a_3$ nucleons, respectively. This implies that $a = a_2 + a_3$. In this case, another Jacobi coordinate needs to be introduced, corresponding to the vector between the two small clusters,

$$\vec{\nu} = \sqrt{\frac{1}{2}}\left[\frac{1}{a_2}\sum_{i=A-a+1}^{A}\vec{r}_i - \frac{1}{a_3}\sum_{i=A-a_3+1}^{A}\vec{r}_i\right].$$

This system is shown in the lower panel in Fig. 3.1. The third cluster with $a_3$ nucleons requires also additional quantum numbers $I_3T_3$ and it is now possible to define a three-body cluster overlap function:

$$\begin{aligned} &u^{A\lambda JT}_{(A-a)I_1T_1,a_2I_2T_2,a_3I_3T_3}(\eta,\nu) \\ &= \langle A\lambda JT|\mathcal{A}_{A-a,a_2,a_3}\Phi^{AJT}_{(A-a)I_1T_1,a_2I_2T_2,a_3I_3T_3};\delta_\eta\delta_\nu\rangle. \end{aligned} \tag{3.2}$$

Acting with the three-cluster antisymmetrizer on the $A$-body state to the left, will simply give a combinatorial factor since the $A$-body state is fully antisymmetric. In Appendix A.1 it is shown that the combinatorial factor is $\sqrt{\frac{A!}{(A-a_2-a_3)!a_2!a_3!}}$. The Dirac $\delta$-functions can be expanded in terms of radial

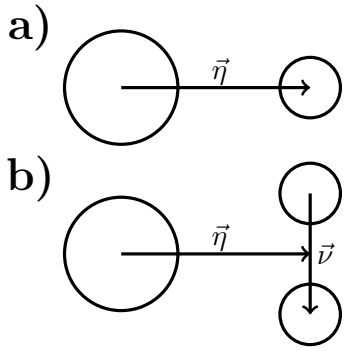


*Figure 3.1: The Jacobi coordinates used in the definition of the overlap functions. a) is the two-body cluster system and b) is the three-body cluster system.*

HO functions and in that way the relative motion can be expressed in a HO basis. We arrive at the expansion in HO functions

$$u^{A\lambda JT}_{a_1 I_1 T_1, a_2 I_2 T_2, a_3 I_3 T_3}(\eta,\nu) = \sqrt{\frac{A!}{(A-a)!a_2!a_3!}} \sum_{\substack{n_\eta l_\eta \\ n_\nu l_\nu}} R_{n_\eta l_\eta}(\eta) R_{n_\nu l\nu}(\nu) \langle A\lambda JT | \Phi^{AJT}_{a_1 I_1 T_1, a_2 I_2 T_2, a_3 I_3 T_3}; n_\eta l_\eta, n_\nu l_\nu \rangle. \tag{3.3}$$

## 3.2 Core-N-N overlap functions

The aim of this section is to derive an expression for the Core+N+N overlap function with matrix elements between many-body states in an SD basis, which can be computed from wave functions obtained in the NCSM. The outline for this derivation is that we will start by introducing three-body cluster wave functions will be introduced in both relative and absolute coordinates. After that the overlap function in relative coordinates will be related to an overlap function in a SD basis. The overlap function will then be expanded and some spin-couplings will be performed. Finally, we can simplify the expanded overlap function and write down the expression for the Core-N-N overlap function.

### 3.2.1 Three-body cluster wave function

The first step is to define the three-body cluster wave function in relative Jacobi coordinates. In the end, the derivation will focus on the Core+N+N channel, where the two smaller clusters consist of only one nucleon each, but as a start we will consider the general case. To treat the entire system microscopically, another set of relative coordinates needs to be introduced to describe the relative distance between the nucleons in each cluster. These coordinates are sets of normalized Jacobi coordinates. In cluster 1 they are defined as

$$\begin{aligned}
\vec{\xi}_1 =& \sqrt{\frac{1}{2}}(\vec{r}_1 - \vec{r}_2) \\
\vec{\xi}_2 =& \sqrt{\frac{2}{3}}\left[\frac{1}{2}(\vec{r}_1 + \vec{r}_2) - \vec{r}_3\right] \\
&\vdots \\
\vec{\xi}_{A-a-1} =& \sqrt{\frac{A-a-1}{A-a}} \\
&\times \left[\frac{1}{A-a-1}(\vec{r}_1 + \vec{r}_2 + \ldots + \vec{r}_{A-a-1}) - \vec{r}_{A-a}\right]
\end{aligned}$$

where $\vec{r}_i$ is the absolute coordinate of particle $i$. The intrinsic coordinates in clusters 2 and 3 are defined in the same way, but denoted $\vec{\mu}_i$ and $\vec{\rho}_i$, respectively. All relative coordinates are shown in Fig. 3.2 for a general example. In the rest of the derivation $\boldsymbol{\xi}$ will be used to denote all $\vec{\xi}_i$ vectors and $\boldsymbol{\mu}$ and $\boldsymbol{\rho}$ will denote the intrinsic coordinates of clusters 2 and 3. A coordinate corresponding to the center of mass of the $A$-body system is also needed

$$\vec{\xi}_0 = \sqrt{\frac{1}{A}}(\vec{r}_1 + \vec{r}_2 + \ldots + \vec{r}_A).$$

The cluster wave function can now be defined in relative coordinates for

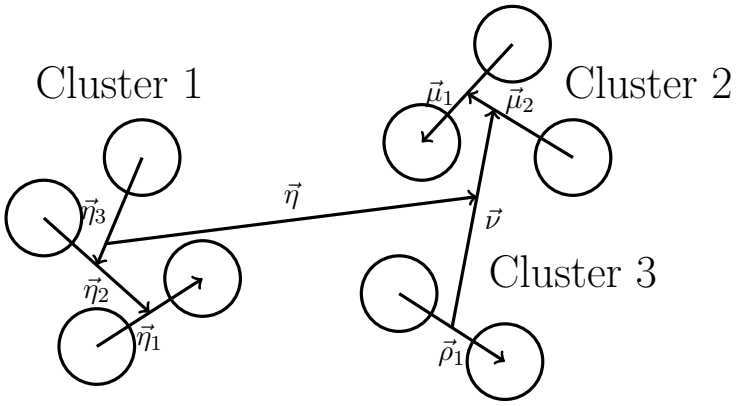


*Figure 3.2: Sketch of the coordinate systems in a three-body cluster system*

a fixed set of relative distances defined by $\eta'$ and $\nu'$

$$\begin{aligned}
\left\langle \boldsymbol{\xi}\eta'\vec{\eta}\boldsymbol{\mu}\nu'\vec{\nu}\boldsymbol{\rho}\boldsymbol{\sigma}\boldsymbol{\tau}\right| \Phi^{AJMTM_T}_{\alpha M_\alpha};\delta_\eta\delta_\nu\Big\rangle &= \sum (l_\eta m_\eta l_\nu m_\nu | LM_L) \\
&\times (I_2 M_2 I_3 M_3 | I_{23} M_{23})(I_1 M_1 I_{23} M_{23} | S M_S)(L M_L S M_S | JM) \\
&\times (T_2 M_{T_2} T_3 M_{T_3} | T_{23} M_{T_{23}})(T_1 M_{T_1} T_{23} M_{T_{23}} | T M_T) \frac{\delta(\eta-\eta')}{\eta\eta'} \frac{\delta(\nu-\nu')}{\nu\nu'} \\
&\times Y_{l_\eta m_\eta}(\hat{\eta}) Y_{l_\nu m_\nu}(\hat{\nu}) \left\langle \boldsymbol{\xi}, \sigma_1 \dots \sigma_{A-a}, \tau_1 \dots \tau_{A-a}\right| a_1 \lambda_1 I_1 M_1 T_1 M_{T_1}\rangle \\
&\times \left\langle \boldsymbol{\mu}, \sigma_{A-a+1} \dots \sigma_{A-a_3} \tau_{A-a+1} \dots \tau_{A-a_3}\right| a_2 \lambda_2 I_2 M_2 T_2 M_{T_2}\rangle \\
&\times \left\langle \boldsymbol{\rho}, \sigma_{A-a_3+1} \dots \sigma_A \tau_{A-a_3+1} \dots \tau_A\right| a_3 \lambda_3 I_3 M_3 T_3 M_{T_3}\rangle ,
\end{aligned} \tag{3.4}$$

where each cluster has a total angular momentum $I_i$, a total isospin $T_i$ and an additional quantum number $\lambda_i$ needed to distinguish the eigenstate. The three clusters together form an $A$-body system with total angular momentum $J$ and a total isospin T, with the projection $M$ and $M_T$, respectively. $\boldsymbol{\sigma} = [\sigma_1, \dots \sigma_A]$ are the spin-coordinates and $\boldsymbol{\tau} = [\tau_1, \dots \tau_A]$ the isospin coordinates. The quantum numbers for the three-cluster state are combined into one index $\alpha = [a_1\lambda_1 I_1 T_1, a_2\lambda_2 I_2 T_2, a_3\lambda_3 I_3 T_3 : LS]$ and $M_\alpha$ is the corresponding set of projection quantum numbers.

In the same manner, it is possible to define a three-body cluster wave

function where the relative motion state is defined by radial HO basis states

$$\begin{aligned}
&\left\langle \boldsymbol{\xi}\eta'\vec{\eta}\boldsymbol{\mu}\nu'\vec{\nu}\boldsymbol{\rho}\boldsymbol{\sigma}\boldsymbol{\tau}\right| \Phi^{AJMTM_T}_{\alpha M_\alpha}; n_\eta l_\eta, n_\nu l_\nu\Big\rangle = \sum (l_\eta m_\eta l_\nu m_\nu | LM_L) \\
&\times (I_2 M_2 I_3 M_3 | I_{23} M_{23})(I_1 M_1 I_{23} M_{23} | S M_S)(L M_L S M_S | J M) \\
&\times (T_2 M_{T_2} T_3 M_{T_3} | T_{23} M_{T_{23}})(T_1 M_{T_1} T_{23} M_{T_{23}} | T M_T) R_{n_\eta, l_\eta}(\eta) R_{n_\nu, l_\nu}(\nu) \\
&\times Y_{l_\eta m_\eta}(\hat{\eta}) Y_{l_\nu m_\nu}(\hat{\nu}) \left\langle \boldsymbol{\xi}, \sigma_1 \ldots \sigma_{A-a}, \tau_1 \ldots \tau_{A-a}\right| a_1 \lambda_1 I_1 M_1 T_1 M_{T_1}\rangle \\
&\times \langle \boldsymbol{\mu}, \sigma_{A-a+1} \ldots \sigma_{A-a_3} \tau_{A-a+1} \ldots \tau_{A-a_3}| \; a_2 \lambda_2 I_2 M_2 T_2 M_{T_2}\rangle \\
&\times \langle \boldsymbol{\rho}, \sigma_{A-a_3+1} \ldots \sigma_A \tau_{A-a_3+1} \ldots \tau_A| \; a_3 \lambda_3 I_3 M_3 T_3 M_{T_3}\rangle \, .
\end{aligned} \tag{3.5}$$

Finally, the last three-body cluster wavefunction that needs to be introduced is the one where the large cluster is expressed in sp coordinates. The coordinate corresponding to the distance $\eta$ also needs to be in absolute coordinates, since sp coordinates introduce a dependence on the CM of the large cluster. Therefore, the coordinate $\vec{R}^a_{CM}$ will be used corresponding to the position of the combined CM of cluster 2 and 3. The three-body cluster overlap wave function with mixed coordinates is

$$\begin{aligned}
&\left\langle \vec{r}_1 \ldots \vec{r}_{A-a} \vec{R}^a_{CM} \boldsymbol{\mu}\vec{\nu}\boldsymbol{\rho}\boldsymbol{\sigma}\boldsymbol{\tau}\right| \Phi^{AJMTM_T}_{\alpha M_\alpha}; n_\eta l_\eta, n_\nu l_\nu\Big\rangle_{SD} \\
&= \sum (l_\eta m_\eta l_\nu m_\nu | LM_L) \; (I_2 M_2 I_3 M_3 | I_{23} M_{23})(I_1 M_1 I_{23} M_{23} | S M_S) \\
&\times (L M_L S M_S | J M)(T_2 M_{T_2} T_3 M_{T_3} | T_{23} M_{T_{23}})(T_1 M_{T_1} T_{23} M_{T_{23}} | T M_T) \\
&\times R_{n_\eta, l_\eta}(R^a_{CM}) R_{n_\nu, l_\nu}(\nu) Y_{l_\eta m_\eta}(\widehat{R}^a_{CM}) Y_{l_\nu m_\nu}(\widehat{\nu}) \\
&\times \langle \vec{r}_1 \ldots \vec{r}_{A-a}, \sigma_1 \ldots \sigma_{A-a}, \tau_1 \ldots \tau_{A-a}| \; a_1 \lambda_1 I_1 M_1 T_1 M_{T_1}\rangle_{SD} \\
&\times \langle \boldsymbol{\mu}, \sigma_{A-a+1} \ldots \sigma_{A-a_3} \tau_{A-a+1} \ldots \tau_{A-a_3}| \; a_2 \lambda_2 I_2 M_2 T_2 M_{T_2}\rangle \\
&\times \langle \boldsymbol{\rho}, \sigma_{A-a_3+1} \ldots \sigma_A \tau_{A-a_3+1} \ldots \tau_A| \; a_3 \lambda_3 I_3 M_3 T_3 M_{T_3}\rangle \, .
\end{aligned} \tag{3.6}$$

In order to use the NCSM eigenstates the overlap function needs to be calculated from states expressed in a SD basis. To relate the overlap function in relative coordinates to a overlap function in absolute coordinates, it is possible to use Eq (2.6) on the composite state and on the large cluster state, both in a SD basis. This factors out the CM motion. It is then possible to apply the Talmi-Moshinsky transformation[25] to finally get a relation between the overlap function in relative coordinates to an overlap function in sp coordinates. This derivation is presented in detail in Appendix

A.2. The final result is

$$\begin{aligned}&\left\langle A\lambda JT\right|\mathcal{A}_{A-a,a_2,a_3}\Phi_\alpha^{AJT};n_\eta l_\eta,n_\nu l_\nu\rangle\\&=\frac{{}_{\rm SD}\left\langle A\lambda JT\right|\mathcal{A}_{a_1,a_2,a_3}\Phi_\alpha^{AJT};n_\eta l_\eta,n_\nu l_\nu\rangle_{\rm SD}}{\langle n_\eta l_\eta 00 l_\eta|\,00 n_\eta l_\eta l_\eta\rangle_{\frac{a}{A-a}}},\end{aligned}\tag{3.7}$$

where the denominator is a general HO bracket from the Talmi-Moshinksy transformation. The value of the bracket is [24]

$$\langle n_\eta l_\eta 00 l_\eta|\,00 n_\eta l_\eta l_\eta\rangle_{\frac{a}{A-a}}=(-1)^{l_\eta}\left(\frac{A-a}{A}\right)^{(2n_\eta+l_\eta)/2}.$$

### 3.2.2 Core+N+N overlap function

Until now, the derivation has been for a general three-body cluster state. In the following we will assume that the two smaller clusters (2 and 3), only consist of one nucleon each. To simplify the notation the spin and isospin labels $I_2$ and $I_3$ ($T_2$ and $T_3$) will be kept, although they corresponds to spin (isospin) $\frac{1}{2}$.

Since Eq. (3.7) relates the overlap function with wave functions in sp coordinates and the overlap function used in Eq. (3.3), the derivation can continue from the overlap function in sp coordinates,

$$\begin{aligned}&{}_{\rm SD}\left\langle A\lambda JMTM_T\right|\Phi_{\alpha,M_\alpha}^{AJMTM_T};n_\eta l_\eta,n_\nu l_\nu\Big\rangle_{\rm SD}\\&=\int d\vec{x}\;{}_{\rm SD}\left\langle A\lambda JMTM_T\right|\vec{r}_1\ldots\vec{r}_{A-a}\vec{R}^a_{C.M}\nu\sigma_1\ldots\sigma_A\tau_1\ldots\tau_A\Big\rangle\\&\times\left\langle\vec{r}_1\ldots\vec{r}_{A-a}\vec{R}^a_{C.M}\nu\sigma_1\ldots\sigma_A\tau_1\ldots\tau_A\right|\Phi_{\alpha,m_\alpha}^{AJMTM_T};n_\eta l_\eta,n_\nu l_\nu\Big\rangle_{\rm SD}\end{aligned}\tag{3.8}$$

The last bracket corresponds to the cluster wave function defined in Eq. 3.6.

The Talmi-Moshinsky transformation, can be used to transform two HO states in relative coordinates to two HO states in sp coordinates,

$$\begin{aligned}&\sum_{m_\eta m_\nu}(l_\eta m_\eta l_\nu m_\nu|LM_L)\left\langle\vec{R}^a_{CM}\right|n_\eta l_\eta m_\eta\Big\rangle\langle\vec{\nu}|\,n_\nu l_\nu m_\nu\rangle\\&=\sum_{\substack{n_a l_a m_a\\ n_b l_b m_b}}\langle n_a l_a n_b l_b L|\,n_\eta l_\eta n_\nu l_\nu L\rangle_1\,(l_a m_a l_b m_b|LM_L)\\&\quad\times\langle\vec{r}_A|\,n_a l_a m_a\rangle\,\langle\vec{r}_{A-1}|\,n_b l_b m_b\rangle\end{aligned}\tag{3.9}$$

where subscripts $a$ and $b$ correspond to two sp states. The summation over sp quantum numbers is constrained by energy conservation. By applying this transformation to the cluster wave function in Eq. (3.8) and re-couple the spins from $LS$-coupling to $j_a j_b$-coupling Eq (3.8) can be written as

$$
\begin{aligned}
&{}_{\rm SD}\Big\langle A\lambda JMTM_T\Big|\ \Phi^{AJMTM_T}_{\alpha,M_\alpha}; n_\eta l_\eta, n_\nu l_\nu\Big\rangle_{\rm SD} \\
&\quad= \int d\vec{x}\,\langle A\lambda JMTM_T|\ \vec{r}_1\ldots\vec{r}_{A-2}\vec{r}_{A-1}\vec{r}_A\nu\sigma_1\ldots\sigma_A\tau_1\ldots\tau_A\rangle \\
&\quad\times\sum(-1)^{I_2+I_3-S+L+I_{23}+I_1+J}\hat{S}\hat{J}_{ab}\begin{Bmatrix} L & I_{23} & J_{ab}\\ I_1 & J & S\end{Bmatrix}\begin{Bmatrix} l_a & l_b & L\\ I_3 & I_2 & I_{23}\\ j_a & j_b & J_{ab}\end{Bmatrix} \\
&\quad\times(-1)^{I_2+I_3-I_{23}+T_2+T_3-T_{23}}\hat{L}\hat{J}_{ab}\hat{j}_a\hat{j}_b(j_a m_{j_a} j_b m_{j_b}|J_{ab}M_{ab}) \\
&\quad\times(J_{ab}M_{ab}I_1M_1|JM)(T_3M_{T_3}T_2M_{T_2}|T_{23}M_{T_{23}})(T_1M_{T_1}T_{23}M_{T_{23}}|TM_T) \\
&\quad\times\langle\vec{r}_1\ldots\vec{r}_{A-2},\sigma_1\ldots\sigma_{A-2},\tau_1\ldots\tau_{A-2}|\ (A-2)\lambda_1 I_1 M_1 T_1 M_{T_1}\rangle \\
&\quad\times\langle n_a l_a n_b l_b L|\ n_\eta l_\eta n_\nu l_\nu L\rangle_1\,(l_b m_b I_2 M_2|j_b m_{j_b})\,\langle\vec{r}_{A-1}|\ n_b l_b m_b\rangle \\
&\quad\times\langle\sigma_{A-1}\tau_{A-1}|\ \lambda_2 I_2 M_2 T_2 M_{T_2}\rangle\,(l_a m_a I_3 M_3|j_a m_{j_a}) \\
&\quad\times\langle\vec{r}_A|\ n_a l_a m_a\rangle\,\langle\sigma_A\tau_A|\ \lambda_3 I_3 M_3 T_3 M_{T_3}\rangle
\end{aligned}
\tag{3.10}
$$

The coordinates of the composite wave function in Eq. (3.10) can be written as a set of field creation operators acting on a vacuum state

$$
\begin{aligned}
&|\vec{r}_1\ldots\vec{r}_A\sigma_1\ldots\sigma_A\tau_1\ldots\tau_A\rangle \\
&\quad=\sum_{\substack{n'_1l'_1j'_1t'_1\\ \vdots\\ n'_Al'_Aj'_At'_A}}\frac{1}{\sqrt{A!}}\,\langle n'_1l'_1j'_1t'_1|\ \vec{r}_1\sigma_1\tau_1\rangle\ldots\langle n'_Al'_Aj'_At'_A|\ \vec{r}_A\sigma_A\tau_A\rangle\,a^\dagger_{n'_1l'_1j'_1t'_1}\ldots a^\dagger_{n'_Al'_Aj'_At'_A}|0> \\
&\quad=\sum_{\substack{n'_{A-1}l'_{A-1}j'_{A-1}t'_{A-1}\\ n'_Al'_Aj'_At'_A}}\sqrt{\frac{(A-2)!}{A!}}\,\langle n'_{A-1}l'_{A-1}j'_{A-1}t'_{A-1}|\ \vec{r}_{A-1}\sigma_{A-1}\tau_{A-1}\rangle \\
&\quad\times\langle n'_Al'_Aj'_At'_A|\ \vec{r}_A\sigma_A\tau_A\rangle\,a^\dagger_{n'_{A-1}l'_{A-1}j'_{A-1}t'_{A-1}}a^\dagger_{n'_Al'_Aj'_At'_A}\,|\vec{r}_1\ldots\vec{r}_{A-2}\sigma_1\ldots\sigma_{A-2}\tau_1\ldots\tau_{A-2}\rangle
\end{aligned}
\tag{3.11}
$$

where $\langle\vec{r}\sigma\tau|\ nljt\rangle$ is a HO wave function with coordinates $\vec{r},\sigma$ and $\tau$. The next step is to insert Eq. (3.11) expression in Eq. (3.10) and identify that the sp states are coupled together to a total spin $j_a$ and $j_b$, respectively. The quantum numbers that are summed over in Eq. (3.11) can be determined

due to the fact that sp states are orthogonal. By applying these operations we can now write an expression for the overlap function in a SD basis,

$$
\begin{aligned}
&{}_{\rm SD}\big\langle A\lambda JMTM_T\big|\ \Phi^{AJMTM_T}_{\alpha,m_\alpha}; n_\eta l_\eta, n_\nu l_\nu\big\rangle_{\rm SD} \\
&= \sum (-1)^{I_2+I_3-S+L+I_{23}+I_1+J}\hat{S}\hat{J}_{ab}
\begin{Bmatrix} L & I_{23} & J_{ab} \\ I_1 & J & S \end{Bmatrix}
\begin{Bmatrix} l_a & l_b & L \\ I_3 & I_2 & I_{23} \\ j_a & j_b & J_{ab} \end{Bmatrix} \\
&\times (-1)^{I_2+I_3-I_{23}+T_2+T_3-T_{23}}\hat{L}\hat{J}_{ab}\hat{j}_a\hat{j}_b\,\langle n_a l_a n_b l_b L|\ n_\eta l_\eta n_\nu l_\nu L\rangle_1 \\
&\times (J_{ab}M_{ab}I_1M_1|JM)(T_1M_{T_1}T_{ab}M_{T_{ab}}|TM_T) \\
&\times \left\langle A\lambda JMTM_T\right| \left[a^\dagger_{n_a l_a j_a t_a} a^\dagger_{n_b l_b j_b t_b}\right]^{J_{ab}M_{ab},T_{ab}M_{T_{ab}}} \left|(A-2)\lambda_1 I_1 M_1 T_1 M_{T_1}\right\rangle .
\end{aligned}
\tag{3.12}
$$

Inserting this expression in Eq. (3.7), and applying the Wigner-Eckart theorem, it is finally possible to write down the reduced expression for the three-body cluster overlap function defined in Eq. (3.3)

$$
\begin{aligned}
u^{A\lambda JT}_\alpha(\eta,\nu) = \sum_{\substack{n_\eta l_\eta \\ n_\nu l_\nu \ldots}} &\frac{R_{n_\eta l_\eta}(\eta)R_{n_\nu l_\nu}(\nu)}{\langle n_\eta l_\eta 00 l_\eta|\ 00 n_\eta l_\eta l_\eta\rangle_{\frac{2}{A-2}}}(-1)^{3I_1+I_{23}+J_{ab}-T_{23}-S+L} \\
&\times \langle n_a l_a n_b l_b L|\ n_\eta l_\eta n_\nu l_\nu L\rangle_1 \frac{\hat{L}\hat{S}\hat{J}^2_{ab}\hat{j}_a\hat{j}_b}{\hat{J}\hat{T}}
\begin{Bmatrix} L & I_{23} & J_{ab} \\ I_1 & J & S \end{Bmatrix}
\begin{Bmatrix} l_a & l_b & L \\ I_3 & I_2 & I_{23} \\ j_a & j_b & J_{ab} \end{Bmatrix} \\
&\times {}_{\rm SD}\left\langle A\lambda JT\right\|\left[a^\dagger_{n_a l_a j_a t_a} a^\dagger_{n_b l_b j_b t_b}\right]^{J_{ab}T_{ab}}\|(A-2)\alpha_1 I_1 T_1\Big\rangle_{\rm SD},
\end{aligned}
\tag{3.13}
$$

where the last matrix element is a reduced non-diagonal transition density computed from microscopic wave functions obtained in the NCSM. This matrix element can be computed with the existing transition density code, TRDENS[26].

## 3.3 Clusterization of $^6$He

We are now in a position were we can analyse the clusterization of $^6$He by computing the overlap function between $^6$He and an antisymmetric three-cluster state consisting of $^4$He and two neutrons. This gives us the possibility to study the cluster structure inherent in the microscopically calculated wave functions. In this section the main results presented in Paper 1, will be shown and discussed.

### 3.3.1 Overlap functions

There are two different spin-channels for the overlap $\langle ^6\mathrm{He}(0^+)|^4\mathrm{He}(0^+)+n+n\rangle$, namely $S = L = 0$ and $S = L = 1$. Recall that $S$ is obtained by coupling together $I_1$, $I_2$ and $I_3$, and $L$ by coupling $l_\eta$ and $l_\nu$. The overlap functions for these two different channels are shown in Fig. 3.1. The most obvious thing to note is that the $S = L = 0$ channel is clearly dominating. This channel also possesses the characteristic shape of the two-neutron Borromean halo with a di-neutron and a cigar configuration. The di-neutron configuration corresponds to that the two neutrons are close together but far away from the core, while in the cigar configuration the neutrons are far from each other but their CM is close to the core. This is in agreement with earlier phenomenological cluster model calculations [3] and microscopic calculations done with a schematic interaction [27].

Very importantly, with this toolbox that we have developed it is now possible to study the origin of the observed clusterization. In Fig. 3.4 the overlap functions obtained in different $N_{\max}$ truncated model spaces are displayed. The panel in the top-left corner corresponds to a really tiny model space, $N_{\max} = 2$, but already here the clusterization is clearly visible. Compared to the panel in the bottom-left corner with a very large model space, $N_{\max} = 14$, there are no distinct differences in the structure. The only visible difference is that the overlap function in the larger model space has a larger radial extension. The conclusion drawn from these results is that the clusterization is driven by the Pauli principle, since in the tiny model space the only property of the wave function that is guaranteed to be captured is the antisymmetrization of the nucleons due to the SD basis. Note that the $N_{\max} = 2$ model space is much too small to capture the physics of the interaction.

### 3.3.2 Spectroscopic factors

An integrated measure of the amount of clusterization is the spectroscopic factor, which is the norm of the squared overlap function. It is worth reminding the reader that spectroscopic factors are non-observable quantities that change, e.g. under unitary transformations of the Hamiltonian. However, they are still important in phenomenological reaction theory as input for taking into account the structure of the atomic nuclei [29].

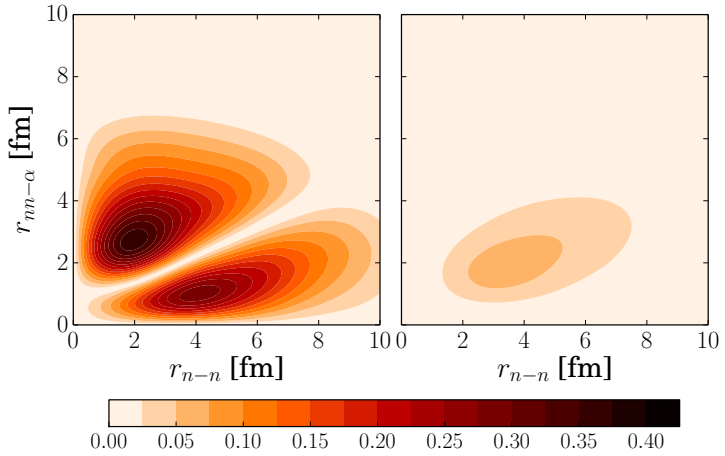


*Figure 3.3: Contour plot of the overlap function of $^6$He. The left (right) panel corresponds to the $S = L = 0$ ($S = L = 1$) channel. This calculation is performed in a NCSM model space with $\hbar\Omega = 20$ MeV and $N_{\max} = 14$ . The interaction is I-N3LO with $\Lambda_{\mathrm{SRG}} = 2.0$ fm$^{-1}$.*

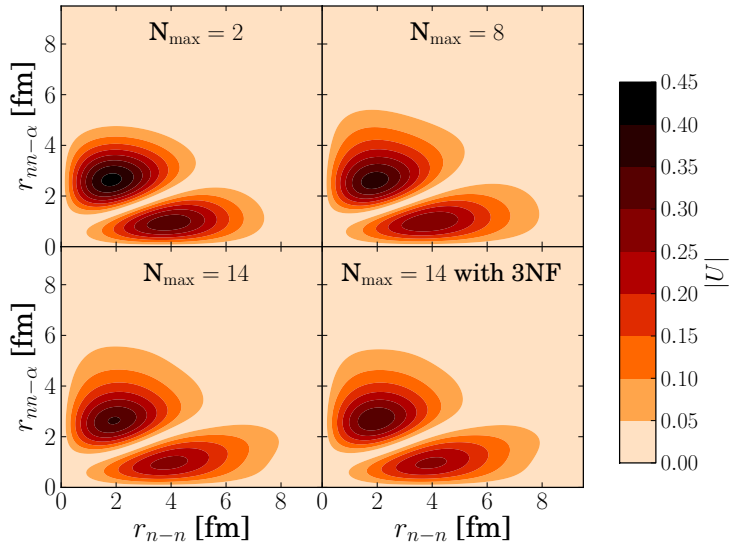


*Figure 3.4: The overlap function for the $S = L = 0$ channel. The wave functions are computed for increasing model spaces with $\hbar\Omega = 16$ MeV and I-N3LO with $\Lambda_{\mathrm{SRG}} = 2.0$ fm$^{-1}$. The wave functions obtained from a Hamiltonian including NN+3NF interactions are provided by R. Roth [28].*

### Projection on a hyperspherical harmonics basis

In order to study the spectroscopic factors we have chosen to project the overlap functions onto a hyperspherical harmonics (HH) basis. This is done by first transforming to hypercoordinates $(\rho, \theta, \hat{\eta}, \hat{\nu})$ where $\eta = \rho\cos(\theta)$ and $\nu = \rho\sin(\theta)$. The overlap function in Eq. (3.13) can be written in hyperspherical coordinates,

$$u_\alpha^{A\lambda JT}(\theta,\rho) = \frac{1}{\rho^{5/2}} \sum_{K,l_\eta,l_\nu} \chi^{A\lambda JT}_{\alpha,Kl_\eta l_\nu}(\rho)\psi_K^{l_\eta l_\nu}(\theta) \tag{3.14}$$

where

$$\begin{aligned}\chi^{A\lambda JT}_{\alpha,Kl_\eta l_\nu} &= \rho^{5/2}\int_0^{\pi/2} d\theta' \sin^2\theta' \cos^2\theta' \psi_K^{l_\eta l_\nu}(\theta) \\ &\times \sum_{n_\eta,n_\nu} C^{A\lambda JT}_{\alpha,n_\eta l_\eta,n_\nu l_\nu} R_{n_\eta l_\eta}(\theta',\rho) R_{n_\nu l_\nu}(\theta',\rho).\end{aligned} \tag{3.15}$$

The $\psi_K^{l_\eta l_\nu}(\theta)$ are the hyperangular basis functions [30] and $K$ is the hyperangular momentum, which can be written as $K = l_\eta + l_\nu + 2n$ where $n = 0, 1, 2 \ldots$. The factor $C^{A\lambda JT}_{\alpha,n_\eta l_\eta,n_\nu l_\nu}$ contains all factors in Eq. (3.13) except the radial HO functions. The projection onto HH basis is presented in further details in App. A.3.

### Results

In Table 3.1 the weights for the five most important terms in the HH expansion are presented, together with the total spectroscopic factor. The first observation from this data is that the dominant term is the $K = 2$ and $l_\eta = l_\nu = 0$ one, in agreement with earlier calculations [27, 3]. This term is responsible for the characteristic two-peak structure shown in Fig. 3.3. One detail that is important to note is that our total spectroscopic factors are larger then one. This is in agreement with the spectroscopic factors computed in a microscopic model presented in [27]. According to Timofeyuk [31] the fact that the spectroscopic factor is larger then unity is due to the movement of the CM of the cluster wavefunction and in Ref. [31] an upper limit of the spectroscopic factor for this system was derived to be $\frac{25}{16} \approx 1.56$, which is consistent with our results. In the cluster calculation [3], the wave functions are normalized with respect to the CM motion, therefore the spectroscopic factors sum up to unity.

*Table 3.1: Relative weights (in %) of the HH expansion terms for the three-body channel form factor $\langle {}^6He(0^+)|{}^4He(0^+)+n+n\rangle$ calculated from NCSM wave functions. We compare results obtained with Hamiltonians including two-body forces only, and with two- plus three-body forces. The last row shows the total spectroscopic factor. We have used: I-N3LO, $\Lambda_{\mathrm{SRG}} = 2.0$ $fm^{-1}$, $\hbar\Omega = 20$ $MeV$ and $N_{\max} = 14$. The 3NF wave function is computed with $\hbar\Omega = 16$ $MeV$ and is provided by R. Roth [28].*

| Three-body channel | | | This work | | Ref. [3] | Ref. [27] |
|---|---|---|---|---|---|---|
| $K$ | $l_\eta = l_\nu$ | $L = S$ | NN | NN+3NF | (cluster) | (microscopic) |
| 0 | 0 | 0 | 4.3 | 4.1 | 4.2 | 4.0 |
| 2 | 0 | 0 | 91.9 | 91.3 | 82.1 | 79.9 |
| 2 | 1 | 1 | 2.2 | 3.0 | 11.2 | 13.3 |
| 6 | 2 | 0 | 1.1 | 1.0 | 1.7 | 1.9 |
| 6 | 3 | 1 | 0.1 | 0.1 | 0.8 | 0.8 |
| Spectroscopic factor: | | | 1.3340 | 1.3284 | 0.9851 | 1.3957 |

In Table 3.2 the spectroscopic factors and the relative weights are displayed for different $\Lambda_{\mathrm{SRG}}$-parameters and HO frequencies. There is clearly a dependence on both $\Lambda_{\mathrm{SRG}}$ and $\hbar\Omega$. However, it is rather small; less then few percent. The overlap function is also computed from wave functions obtained with a Hamiltonian including three-body forces [28]. The overlap function is shown in Fig. 3.4 (lower-right panel) and the spectroscopic function is listed in Tab. 3.1. The result indicates no distinct difference compared to the results including only two-body forces.

The dependence on $\hbar\Omega$ can also be studied by plotting the hyperradial overlap function. In the lower panel of Fig. 3.5, the hyperradial function is plotted for a range of HO frequencies and what we can observe is that different HO frequencies result mainly in changes in the outer part of the overlap function. This is what we expect since the outer region of the overlap function is the most difficult part to converge in a HO basis and will be sensitive to the HO length. The problem with converging the outer part of the overlap function is even more clearly seen in the upper panel of Fig. 3.5, where the hyperradial functions are plotted for $N_{\max} = 14$ and $N_{\max} = 12$. In this panel it is clearly visible that the outer part of the overlap function is not yet converged. The tail is building up slowly between $N_{\max} = 12$ and $N_{\max} = 14$. Since we are limited to model spaces up to $N_{\max} = 14$ we will not be able to reproduce the asymptotic behaviour expected for a loosely bound

*Table 3.2: Relative weights (in %) of the HH expansion terms for the three-body channel form factor $\left\langle {}^6He(0^+)|{}^4He(0^+)+n+n\right\rangle$ calculated from NCSM wave functions. The last row shows the total spectroscopic factor. I-N3LO with $N_{\max}=14$.*

| Three-body channel | | | This work ($\Lambda_{\mathrm{SRG}}$ [fm$^{-1}$],$\hbar\Omega$ [MeV]) | | | | |
|---|---|---|---|---|---|---|---|
| $K$ | $l_\eta = l_\nu$ | $L=S$ | $(1.8, 20)$ | $(2.0, 16)$ | $(2.0, 20)$ | $(2.0, 22)$ | $(2.2, 20)$ |
| 0 | 0 | 0 | 4.2 | 4.4 | 4.3 | 4.2 | 4.3 |
| 2 | 0 | 0 | 92.0 | 91.7 | 91.9 | 92.1 | 92.0 |
| 2 | 1 | 1 | 2.1 | 2.1 | 2.2 | 2.2 | 2.2 |
| 6 | 2 | 0 | 1.1 | 1.2 | 1.1 | 1.0 | 1.0 |
| 6 | 3 | 1 | 0.1 | 0.1 | 0.1 | 0.1 | 0.1 |
| Spectroscopic factor: | | | 1.3441 | 1.3263 | 1.3340 | 1.3391 | 1.3278 |

three-body system. The expected form is

$$\chi(\rho) \sim \exp(-\kappa\rho),$$

where $\kappa^2\hbar^2/2m = S$ and $S$ is the separation energy [3]. For a proper treatment of the outer part of the overlap function also the continuum needs to be taken into account. There are ongoing projects to include the continuum, for example with the NCSM/resonating group metod (NCSM/RGM)[32]. However, we stress that the norms and the relative weights are mostly determined by the interior part of the overlap function.

We are also in the position that we can compute overlap functions between excited states. In Table 3.3 the relative weights and the spectroscopic factors for the overlap function $\left\langle {}^6\mathrm{He}(0^+)|{}^4\mathrm{He}(2^+)+n+n\right\rangle$ are presented. The $^4$He$(2^+)$ is at rather high excitation energy and has rather slow convergence in NCSM. The state is situated below the $2p+2n$ threshold. The total spectroscopic factor is 0.29, which is not negligible.

## 3.4 Clusterization of $^6$Li

Our method can also be used to study other clustered systems. One system that already has been studied in the two-body cluster overlap framework is $^6$Li$(1^+)$ [24]. In that framework it was considered as a system consisting of $^4$He and a deuteron, and the overlap $\left\langle {}^6\mathrm{Li}(1^+)|{}^4\mathrm{He}(0^+)+{}^2\mathrm{H}\right\rangle$ was computed. In our three-body framework it will be studied as $^4$He and two independent

*Table 3.3: Relative weights (in %) of the HH expansion terms for the three-body overlap function* $\left\langle {}^6He(0^+)|{}^4He(2^+)+n+n\right\rangle$. *I-N3LO with* $N_{\max}=14$, $\hbar\Omega=20$ *MeV and* $\Lambda_{\mathrm{SRG}}=2.0$ $fm^{-1}$. *The last row is the total spectroscopic factor.*

| Three-body channel | | | | This work |
|---|---|---|---|---|
| $K$ | $l_\nu$ | $l_\eta$ | $L=S$ | |
| 2 | 0 | 2 | 2 | 54.7 |
| 2 | 2 | 0 | 2 | 36.8 |
| 4 | 2 | 0 | 2 | 3.3 |
| 4 | 0 | 2 | 2 | 3.1 |
| 6 | 4 | 2 | 2 | 0.6 |
| Spectroscopic factor: | | | | 0.2904 |

*Table 3.4: Relative weights (in %) of the HH expansion terms of the three-body overlap function* $\left\langle {}^6Li(1^+)|{}^4He(0^+)+n+p\right\rangle$. $N_{\max}=14$,$\hbar\Omega=20$ *MeV and* $\Lambda_{\mathrm{SRG}}=2.0$ $fm^{-1}$. *The last row is the total spectroscopic factor.*

| Three-body channel | | | | | This work |
|---|---|---|---|---|---|
| $K$ | $l_\nu$ | $l_\eta$ | $S$ | $L$ | |
| 2 | 0 | 0 | 1 | 0 | 87.8 |
| 0 | 0 | 0 | 1 | 0 | 4.9 |
| 2 | 1 | 1 | 0 | 1 | 4.2 |
| 4 | 0 | 0 | 1 | 0 | 1.5 |
| 4 | 2 | 0 | 1 | 2 | 1.3 |
| Spectroscopic factor: | | | | | 1.4015 |

nucleons, one proton and one neutron. The overlap functions of the four possible SL channels are displayed in Fig. 3.6. The $S=1$ $L=0$ channel is the clearly dominating one. The relative weights and the total spectroscopic factor are listed in Table 3.4. What is worth noting is that the dominating channel, $S=1$, $L=0$ (with $l_\nu=0$) corresponds to the S-wave part of the deuteron. Also the D-wave component appears in the last row, which is characterized by $l_\nu=2$.

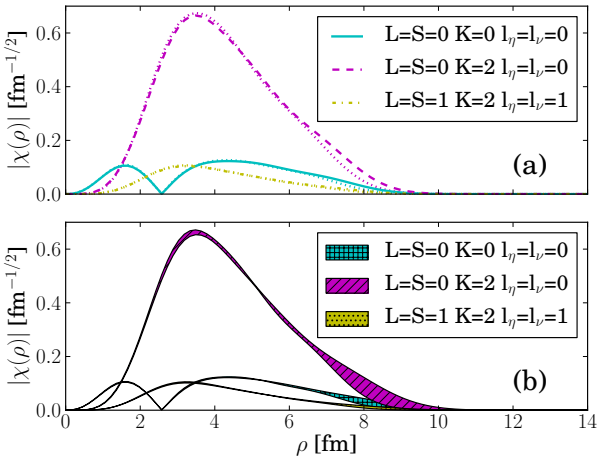


*Figure 3.5: Hyperradial function of the most important terms in the HH expansion. I-N3LO with* $\Lambda_{\mathrm{SRG}} = 2.0\ fm^{-1}$. *(a)* $N_{\max}$ *dependence for a fixed frequency* $\hbar\Omega = 20$ *MeV. Thick lines correspond to* $N_{\max} = 14$ *results, while dotted ones are* $N_{\max} = 12$. *(b) A fixed model space (*$N_{\max} = 14$*) and a range of HO frequencies,* $\hbar\Omega \in [16, 22]$ *that corresponds to the shaded bands.*

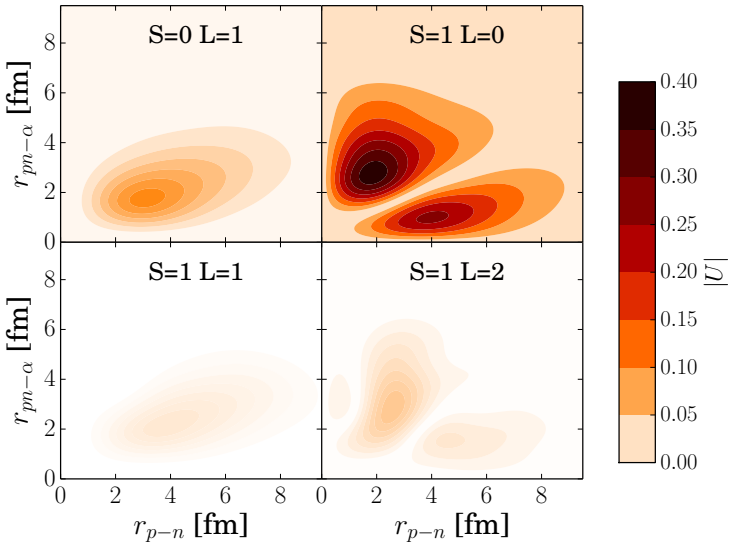


*Figure 3.6: The four possible channels in the three-body overlap* $\langle {}^6Li(1^+)|{}^4He(0^+) + n + p\rangle$. *Computed in a* $N_{\max} = 14$ *model space with* $\hbar\Omega = 20$ *MeV and with I-N3LO interaction evolved to* $\Lambda_{\mathrm{SRG}} = 2.0\ fm^{-1}$.

# Chapter 4

# Core swelling in $^6$He

In a cluster model of a halo system the core is treated as an inert particle. However, one could imagine that the core inside the halo is different from the corresponding free particle. It could get affected by the medium. In particular, the radius of the core is a property which may be affected since the nucleons in the core will feel an attractive force from the valence nucleons. This effect is called core and is treated in different ways in different cluster models. One example is the work of Zhukov et al. [3], where the $V_{n-\alpha}$ interaction was modified to obtain the correct binding energy by increasing the phenomenological parameter associated with the $^4$He radius. Another example is in Ref. [33] where Papadimitriou et al. solved the three-body problem taking into account the continuum, but calculated the charge radius of $^6$He using a manually enlarged core radius. In contrast to cluster models a microscopic model treats all the nucleons on the same footing and no simplifications need to be done regarding the core. Therefore, it is in principle possible to study the core swelling in a microscopic model. The challenge is to extract the relevant information from the multi-dimensional wave function. One important thing to note is that the main difference in charge radius between the halo nucleus and the core nucleus is due to that the CM of the two systems are different.

## 4.1 Proton-proton distance

In the NCSM we have the ability to compute translationally invariant wave functions and should be able to study the core. One way of quantifying the

amount of core swelling in a neutron halo system is to compute the average distance between the protons, $r_{pp}$, in the core and compare that with the same distance computed for the core nucleus without the valence neutrons. In $^6$He this corresponds to a comparison of the distance between the two protons and the distance corresponding distance in $^4$He. The $\hat{r}^2_{pp}$ operator is a two-body operator only acting on two-body proton states. It is possible to write a two-body operator in the second quantization formalism and expand the operator in single-particle states [6]. Schematically, what we need to compute is

$$\begin{aligned}\left\langle A\lambda JT\right| \hat{r}^2_{pp} \left|A\lambda JT\right\rangle = \sum_{a,b,c,d} C^{A\lambda JT}_{ab,cd} \\ \times \left\langle ab\right| \hat{r}^2_{pp} \left|cd\right\rangle \left\langle A\lambda JT\right| \left[\left[a^\dagger_a a^\dagger_b\right] \left[a_c a_d\right]\right] \left|A\lambda JT\right\rangle ,\end{aligned} \tag{4.1}$$

where $a$, $b$, $c$ and $d$ are sp proton states. To simplify the notation all normalization and spin-coupling coefficients are compactified into $C^{A\lambda JT}_{ab,cd}$. In practice, to compute the two-body matrix elements, $\left\langle ab\right| r^2_{pp} \left|cd\right\rangle$, we can use the fact that the potential term in a relative HO Hamiltonian is proportional to the relative distance between two nucleons. By subtracting the relative kinetic energy from the HO Hamiltonian it is simple to obtain these two-body matrix elements in a HO basis. The transition density matrix element $\left\langle A\lambda JT\right| \left[\left[a^\dagger_a a^\dagger_b\right] \left[a_c a_d\right]\right] \left|A\lambda JT\right\rangle$ can be computed from wave functions obtained in the NCSM, with the existing transition density code, TRDENS[26]. Results for $^6$He and $^4$He are shown in Fig. 4.1 where the $r_{pp}$ is presented as a function of $N_{\max}$ for a number of HO frequencies. The pp distances $^6$He and $^4$He are marked with triangles and circles, respectively. To obtaine these is a computationally challenging task. It requieres to find all allowed combinations of two-body states that can be annihilated and created in a huge many-body basis. For the moment, the existing code is limiting which calculations we are able to do. Therefore, the results, in particular for $^6$He, are not fully converged. However, the core swelling is clearly visible. The ratio between the $r_{pp}$ distances in $^6$He and in $^4$He are also presented in Fig. 4.1. The core swelling seems to converge to something in the range of $5-6\%$.

Pieper et al. [34], computed the core swelling with a Quantum Monte Carlo method, and the AV18 interaction, by comparing the proton-proton distribution in the core. They observed a core swelling effect of approximately 4%, which is comparable to our results. One effect that may contribute to the core swelling is the isospin charge-exchange part of the interaction, which

can transfer charge from the core to the valence nucleons [34]. This effect will also cause an enlarged $r_{pp}$ distance and how important its importance needs to be investigated further.

## 4.2 Two- and n-body transition densities

To overcome the limitations in the existing code, TRDENS a code development project has been initialised. The current aim is to improve the computational algorithm for obtaining one- and two-body transition densities, which can be used to calculate expectation values for one- and two-body operators, as well as off-diagonal transition matrix elements from e.g. two-body currents. The derivations behind the computation of coupled one- and two-body transition densities are presented in App. B. In the long-run the aim is to be able to compute also three- and four-body transition densities. The main features of our new code, preliminary named ANICR, are: (i) ANICR an improved algorithm to optimize the search for possible combinations of two-body states and minimize the number of times Clebsch-Gordan coefficients are computed, and (ii) the use of hash tables in a more efficient way. In Fig. 4.2 a preliminary benchmark comparison is presented for the TRDENS and ANICR. The figure shows the timing of computing coupled two-body transition densities for a number of different nuclei in various model spaces. The computations are done in serial on a 2 GHz Sandy Bridge processor. The matrix elements have the form $a_a^\dagger a_b^\dagger a_c a_d$. What is clearly visible is that ANICR is already faster and more efficient. In $^4$He, the largest model space that is possible to compare is $N_{\max} = 12$, where ANICR is 14.9 times faster then TRDENS. The ratio in case of $^6$He is of the same order of magnitude.

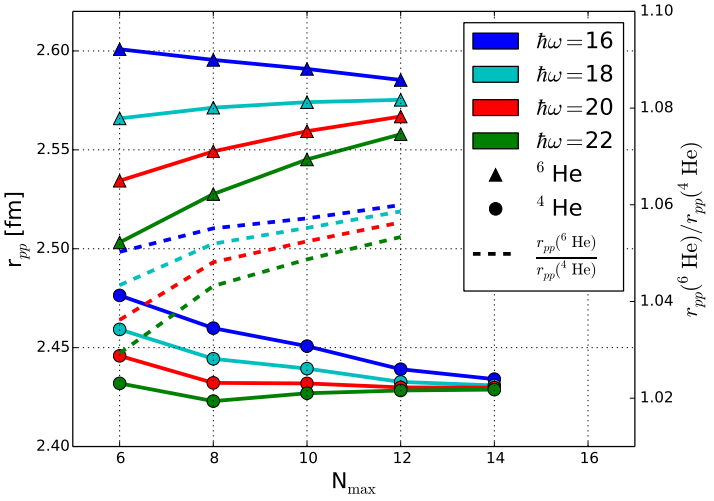


*Figure 4.1: The $r_{pp}$ distance (continues lines) in $^4$He and $^6$He. The core swelling in percent (dashed lines) is also shown. These calculations are done with I-N3LO and $\Lambda_{\mathrm{SRG}} = 2.0$ fm$^{-1}$*

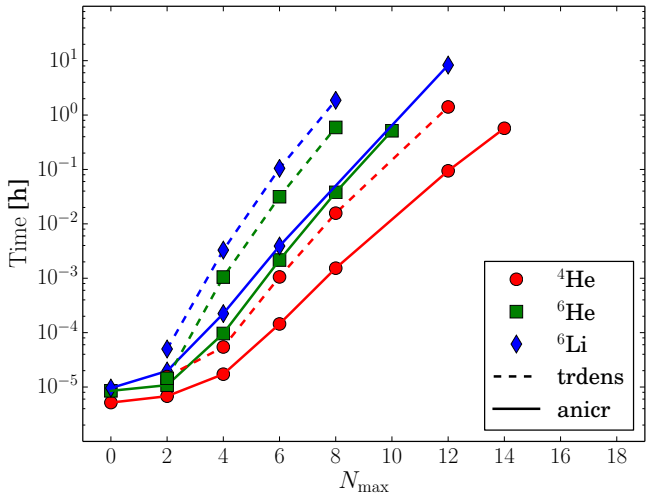


*Figure 4.2: Timing results comparing* ANICR *and* TRDENS*, computing two-body transition densities on a single thread with a 2.0 GHz Sandy-Bridge processor [35].*

# Chapter 5

# Discussion and outlook

In this thesis we have presented nuclear-structure results obtained with the *ab initio* NCSM. We have presented observables for light nuclei such as the ground state energy and the point-proton radius of $^6$He and $^6$Li. Recent code developments allow us to do computations in very large model spaces (for $^6$Li up to $N_{\max} = 22$). We are therefore able to obtain well converged results for A=6 systems with realistic bare interactions.

We also demonstrated a way of correcting our computed results for the finite HO basis we are employing, and showed how this can be used to extrapolate to basis-independent results. However, the choice of the infrared cutoff parameter, $L$, needs to be understood as shortcomings are visible in both the extrapolation of the ground state energy and the radius. The infrared cutoff in the NCSM many-body model space therefore needs to be investigated further. Our large model space calculations are a useful tool in this investigation, since we now can compute converged many-body systems. The outlook is to study the extrapolation further and also extend what observables these corrections can be applicable to.

Furtermore, a framework for studying three-body cluster systems in the NCSM was presented. This toolbox was exemplified by showing how it can be used for studying the clusterization in $^6$He. There are other systems that would be interesting to study in a similar way. One example is the two-neutron halo state in $^{11}$Li. Our formalism requires that we can compute $a^\dagger a^\dagger$-matrix elements. This is limited by the inability of the available transition density code, TRDENS, to compute diagonal and non-diagonal transition density matrix elements in large model spaces.

Finally, we discussed the core swelling effect in a halo system and pre-

sented results for $^6$He where we clearly can observe that the core is enlarged. Again, to be able to compute a converged result we need to extend our capabilities to compute the transition densities in large model spaces. To overcome this problem we have initiated a code development project, under the preliminary name, ANICR. This code will be able to compute one- and two-body transition matrix elements in a more efficient way than existing codes. Preliminary performance data were presented and the outlook seems promising. The code will hopefully open up new possibilities of computing many-body operators in larger model spaces. One opportunity that arises when having access to two-body transition densities is to compute matrix elements for two-body currents in large model spaces. However, the aim is to also include three- and eventually four-body densities. Such densities are needed e.g. in the kernels of NCSM/RGM calculations[36, 32]. Furthermore, one could envision the ability to study effects of nuclear four-body forces in a perturbative approach.

# Appendices

# Appendix A

# Three-body cluster overlap function

## A.1 Cluster Antisymmetrizer

The cluster antisymmetrizer $\mathcal{A}_{a_1,a_2,a_3}$ acting on a three-body cluster system ensures antisymmetrization with respect to the exchange of particles between three clusters. When the antisymmetrizer acts on a cluster state the result is a sum of states consisting of all possible permutations of particles between clusters. For every exchange of two particles from two different clusters the sign changes. The sum needs to be normalized with the total number of cluster permutations. The three-cluster antisymmtrizer is defined as

$$\mathcal{A}_{a_1,a_2,a_3} = \frac{1}{\sqrt{N_3}} \sum_{\text{permutations}} (-1)^{\pi} \prod_{ij} \hat{P}_{ij}, \tag{A.1}$$

where $i, j$ are particles belonging to different clusters, $\hat{P}_{ij}$ is the exchange operator that exchanges particle $i$ and $j$. $a_1$, $a_2$ and $a_3$ are the number of nucleons in cluster 1, 2 and 3, respectively. $\pi$ is the number of exchanges and $N_3$ is the total number of possible permutations. The total number of particle exchanges between three clusters is

$$N_3 = \binom{A}{a_1}\binom{A-a_1}{a_2} = \frac{A!}{(A-a_1)!a_1!}\frac{(A-a_1)!}{a_2!a_3!} = \frac{A!}{a_1!a_2!a_3!}. \tag{A.2}$$

In the derivation presented in Chap. 3 we are acting with the cluster antisymmetrizer on a SD state, which is already antisymmetric with respect

to all particle exchanges. Therefore, every particle exchange will result in a state equal to the SD state and we will in the end have $N_3$ SD states. This can be written as

$$\begin{aligned}\mathcal{A}_{a_1,a_2,a_3} |\Psi(1,\ldots,A)\rangle_{SD} &= \frac{1}{\sqrt{N_3}}(|\Psi(1,\ldots,A)\rangle_{SD} + \ldots + |\Psi(1,\ldots,A)\rangle_{SD}) \\ &= \frac{1}{\sqrt{N_3}} N_3 |\Psi(1,\ldots,A)\rangle_{SD} \,.\end{aligned} \tag{A.3}$$

This gives us that when applying the three-body cluster antisymmetrizer to an antisymmetric SD state, the result is a combinatorial factor,

$$\sqrt{N_3} = \sqrt{\frac{A!}{(A-(a_2+a_3))!a_2!a_3!}}. \tag{A.4}$$

## A.2 Overlap functions: from relative to single-particle coordinates

The derivation of the cluster overlap functions uses the possibility to transform the overlap function from an expression in relative coordinates to an expression in single-particle coordinates. This transformation is essential for the use of wave functions in a SD basis as computed in the NCSM. In this appendix, the relation between a three-body cluster overlap function in Jacobi coordinates and the same overlap function in single-particle coordinates will be derived.

As a starting point of the derivation the three-body cluster wave function needs to be defined. This has been done in Sec. 3.2. The three-body cluster wave function that is used in this derivation is expressed in mixed coordinates, similar to Eq. (3.6). The large cluster, Cluster 1, and the center of mass of the two smaller clusters are expressed in absolute coordinates. The intrinsic motion of cluster 2 and 3 together with their relative motion, $\nu$, are expressed in Jacobi coordinates. The three-body cluster wave function is defined in Eq. (3.6) and is

$$\begin{aligned}
&\left\langle \vec{r}_1 \dots \vec{r}_{A-a} \vec{R}^a_{CM} \boldsymbol{\mu} \vec{\nu} \boldsymbol{\rho} \boldsymbol{\sigma} \boldsymbol{\tau} \right| \Phi^{AJMTM_T}_{\alpha M_\alpha}; n_\eta l_\eta, n_\nu l_\nu \Big\rangle_{SD} \\
&= \sum (l_\eta m_\eta l_\nu m_\nu | L M_L)(I_2 M_2 I_3 M_3 | I_{23} M_{23})(I_1 M_1 I_{23} M_{23} | S M_S) \\
&\quad \times (L M_L S M_S | J M)(T_2 M_{T_2} T_3 M_{T_3} | T_{23} M_{T_{23}})(T_1 M_{T_1} T_{23} M_{T_{23}} | T M_T) \\
&\quad \times R_{n_\nu, l_\nu}(\nu) Y_{l_\nu m_\nu}(\hat{\nu}) \left\langle \vec{R}^a_{CM} \right| n_\eta l_\eta m_\eta \Big\rangle \\
&\quad \times \langle \vec{r}_1 \dots \vec{r}_{A-a}, \sigma_1 \dots \sigma_{A-a}, \tau_1 \dots \tau_{A-a} |\ (A-a) \lambda_1 I_1 M_1 T_1 M_{T_1} \rangle \\
&\quad \times \langle \boldsymbol{\mu}, \sigma_{A-a+1} \dots \sigma_{A-a_3} \tau_{A-a+1} \dots \tau_{A-a_3} |\ \lambda_2 I_2 M_2 T_2 M_{T_2} \rangle \\
&\quad \times \langle \boldsymbol{\rho}, \sigma_{A-a_3+1} \dots \sigma_A \tau_{A-a_3+1} \dots \tau_A |\ \lambda_3 I_3 M_3 T_3 M_{T_3} \rangle \,,
\end{aligned} \tag{A.5}$$

where $R_{n_\eta, l_\eta}(R^a_{CM}) Y_{l_\eta m_\eta}(\hat{R}^a_{CM})$ forms a HO state.

An $A$-body wavefunction in a SD basis consisting of HO states can be defactorized into a part consisting of the CM motion and a part corresponding to the intrinsic motion of the wavefunction,

$$\begin{aligned}
&\langle \vec{r}_1 \dots \vec{r}_A \sigma_1 \dots \sigma_A \tau_1 \dots \tau_A |\ A \lambda J M T M_T \rangle_{S.D.} \\
&= \left\langle \vec{\xi}_1 \dots \vec{\xi}_{A-1} \sigma_1 \dots \sigma_A \tau_1 \dots \tau_A \right| A \lambda J M T M_T \Big\rangle \times \langle R_{CM} |\ 000 \rangle
\end{aligned} \tag{A.6}$$

where the CM is in $0S$ state [37].

By applying this relation to cluster 1 in equation A.5, it is possible to identify two HO states in absolute coordinates, where one is related to the CM motion of cluster 1 and the other one related to the CM motion of cluster 2 and cluster 3.

$$\begin{aligned}
&\left\langle \vec{r}_1 \dots \vec{r}_{A-a} \vec{R}^a_{CM} \boldsymbol{\mu} \vec{\boldsymbol{\nu}} \boldsymbol{\rho} \boldsymbol{\sigma} \boldsymbol{\tau} \right| \Phi^{AJMTM_T}_{\alpha M_\alpha}; n_\eta l_\eta, n_\nu l_\nu \Big\rangle_{S.D} \\
&= \sum (l_\eta m_\eta l_\nu m_\nu | L M_L)(I_2 M_2 I_3 M_3 | I_{23} M_{23})(I_1 M_1 I_{23} M_{23} | S M_S) \\
&\quad \times (L M_L S M_S | J M)(T_2 M_{T_2} T_3 M_{T_3} | T_{23} M_{T_{23}})(T_1 M_{T_1} T_{23} M_{T_{23}} | T M_T) \\
&\quad \times R_{n_\nu, l_\nu}(\nu) Y_{l_\nu m_\nu}(\hat{\nu}) \left\langle \vec{R}^a_{CM} \right| n_\eta l_\eta m_\eta \Big\rangle \left\langle \vec{R}^{A-a}_{CM} \right| 000 \Big\rangle \\
&\quad \times \left\langle \vec{\xi}_1 \dots \vec{\xi}_{A-a}, \sigma_1 \dots \sigma_{A-a}, \tau_1 \dots \tau_{A-a} \right| (A-a) \lambda_1 I_1 M_1 T_1 M_{T_1} \Big\rangle \\
&\quad \times \langle \boldsymbol{\mu}, \sigma_{A-a+1} \dots \sigma_{A-a_3} \tau_{A-a+1} \dots \tau_{A-a_3} |\ \lambda_2 I_2 M_2 T_2 M_{T_2} \rangle \\
&\quad \times \langle \boldsymbol{\rho}, \sigma_{A-a_3+1} \dots \sigma_A \tau_{A-a_3+1} \dots \tau_A |\ \lambda_3 I_3 M_3 T_3 M_{T_3} \rangle \,,
\end{aligned} \tag{A.7}$$

Two HO states with absolute coordinates can be described by two HO states in relative coordinates, where one coordinate describes the CM motion and one coordinate the relative motion between the two HO states. This transformation is called the Talmi-Moshinsky transformation[38] and can be written as

$$\sum_{m_1 m_2} (l_1 m_1 m_2 l_2 | Q q) \langle r_1 |\ n_1 l_1 m_1 \rangle \langle r_2 |\ n_2 l_2 m_2 \rangle \tag{A.8}$$

$$= \sum_{\substack{nlm \\ NLM}} \langle nlNLQ |\ n_1 l_1 n_2 l_2 Q \rangle_D (lmLM | Q q) \langle \vec{r} |\ nlm \rangle \left\langle \vec{R}_{CM} \right| NLM \Big\rangle , \tag{A.9}$$

where subscript 1 and 2 corresponds to two states in absolute coordinates. $\vec{R}$ is the CM coordinate and $\vec{r}$ is the relative coordinate between the two states. $\langle nlNLQ |\ n_1 l_1 n_2 l_2 Q \rangle_D$ is a general HO bracket and D is the mass ratio of the two particles.

In Eq. (A.7) two HO states in absolute coordinates can be identified, $\left\langle \vec{R}^{A-a}_{CM} \right| 000 \Big\rangle \left\langle \vec{R}^a_{CM} \right| n_\eta l_\eta m_\eta \Big\rangle$ and by applying the Talmi-Moshinksy transformation, the two states described by a CM coordinate for the A-body system $\vec{\xi}_0$ and a relative coordinate $\vec{\eta}$ between the combined CM of cluster 1 and the CM of cluster 2 and 3. Therefore, is it now possible to write the three-body

cluster wave function as

$$
\begin{aligned}
&\left\langle \vec{r}_1 \dots \vec{r}_{A-a} \vec{\eta} \boldsymbol{\mu} \vec{\nu} \boldsymbol{\rho} \boldsymbol{\sigma} \boldsymbol{\tau} \right| \Phi^{AJMTM_T}_{\alpha M_\alpha}; n_\eta l_\eta, n_\nu l_\nu \Big\rangle_{S.D} \\
&= \sum (l_\eta m_\eta l_\nu m_\nu | L M_L)(I_2 M_2 I_3 M_3 | I_{23} M_{23})(I_1 M_1 I_{23} M_{23} | S M_S) \\
&\quad \times (L M_L S M_S | J M)(T_2 M_{T_2} T_3 M_{T_3} | T_{23} M_{T_{23}})(T_1 M_{T_1} T_{23} M_{T_{23}} | T M_T) \\
&\quad \times R_{n_\nu, l_\nu}(\nu) Y_{l_\nu m_\nu}(\hat{\nu}) \left\langle \vec{\xi}_1 \dots \vec{\xi}_{A-a}, \sigma_1 \dots \sigma_{A-a}, \tau_1 \dots \tau_{A-a} \right| (A-a) \lambda_1 I_1 M_1 T_1 M_{T_1} \Big\rangle \\
&\quad \times \langle \boldsymbol{\mu}, \sigma_{A-a+1} \dots \sigma_{A-a_3} \tau_{A-a+1} \dots \tau_{A-a_3} |\ \lambda_2 I_2 M_2 T_2 M_{T_2} \rangle \\
&\quad \times \langle \boldsymbol{\rho}, \sigma_{A-a_3+1} \dots \sigma_A \tau_{A-a_3+1} \dots \tau_A |\ \lambda_3 I_3 M_3 T_3 M_{T_3} \rangle \\
&\quad \times \sum_{\substack{n' l' m' \\ N' L' M'}} \left\langle n' l' N' L' l_\eta \right| 00 n_\eta l_\eta l_\eta \Big\rangle_{\frac{a}{A-a}} (l' m' L' M' | l_\eta m_\eta) \left\langle \vec{\eta} \right| n' l' m' \Big\rangle \left\langle \vec{\xi}_0 \right| N' L' M' \Big\rangle ,
\end{aligned}
\tag{A.10}
$$

The relation between an overlap function in absolute coordinates and in relative coordinates can now be derived. By applying Eq. (A.6) to the $A$-body state and the steps performed in Eq. (A.5-A.10) to the cluster state, the overlap function expressed in a SD basis is

$$
\begin{aligned}
&{}_{\mathrm{SD}}\left\langle A \lambda J M T M_T \right| \Phi^{AJMTM_T}_{\alpha, M_\alpha}; n_\eta l_\eta, n_\nu l_\nu \Big\rangle_{\mathrm{SD}} \\
&= \int d\vec{x} \left\langle A \lambda J M T M_T \right| \vec{\xi}_1 \dots \vec{\xi}_{A-1} \sigma_1 \dots \sigma_A \tau_1 \dots \tau_A \Big\rangle \left\langle 000 \right| \vec{\xi}_0 \Big\rangle \\
&\quad \times \sum (l_\eta m_\eta l_\nu m_\nu | L M_L)(I_2 M_2 I_3 M_3 | I_{23} M_{23})(I_1 M_1 I_{23} M_{23} | S M_S) \\
&\quad \times (L M_L S M_S | J M)(T_2 M_{T_2} T_3 M_{T_3} | T_{23} M_{T_{23}}) \\
&\quad \times (T_1 M_{T_1} T_{23} M_{T_{23}} | T M_T) R_{n_\nu, l_\nu}(\nu) Y_{l_\nu m_\nu}(\hat{\nu}) \\
&\quad \times \left\langle \vec{\xi}_1 \dots \vec{\xi}_{A-a}, \sigma_1 \dots \sigma_{A-a}, \tau_1 \dots \tau_{A-a} \right| (A-a) \lambda_1 I_1 M_1 T_1 M_{T_1} \Big\rangle \\
&\quad \times \langle \boldsymbol{\mu}, \sigma_{A-a+1} \dots \sigma_{A-a_3} \tau_{A-a+1} \dots \tau_{A-a_3} |\ \lambda_2 I_2 M_2 T_2 M_{T_2} \rangle \\
&\quad \times \langle \boldsymbol{\rho}, \sigma_{A-a_3+1} \dots \sigma_A \tau_{A-a_3+1} \dots \tau_A |\ \lambda_3 I_3 M_3 T_3 M_{T_3} \rangle \\
&\quad \times \sum_{\substack{n' l' m' \\ N' L' M'}} \left\langle n' l' N' L' l_\eta \right| 00 n_\eta l_\eta l_\eta \Big\rangle_{\frac{a}{A-a}} (l' m' L' M' | l_\eta m_\eta) \left\langle \vec{\eta} \right| n' l' m' \Big\rangle \left\langle \vec{\xi}_0 \right| N' L' M' \Big\rangle .
\end{aligned}
\tag{A.11}
$$

Now the summation in the last row can be simplified. First of all an integration over the $\xi_0$ coordinate can be performed and since the HO functions are orthonormal only $N' = L' = M' = 0$ will contribute. Energy conservation must also be considered in the Talmi-Moshinsky transformation and if

$N' = L' = 0$ the only option is that $n' = n_\eta$, $l' = l_\eta$ and $m' = m_\eta$. The cluster wave function defined in Eq. 3.4 can be identified and finally Eq. (A.12) can be written as an overlap in relative coordinates,

$$\begin{aligned} &{}_{\text{SD}}\left\langle A\lambda JMTM_T \right| \Phi^{AJMTM_T}_{\alpha,M_\alpha}; n_\eta l_\eta, n_\nu l_\nu \Big\rangle_{\text{SD}} \\ &\quad = \left\langle A\lambda JMTM_T \right| \Phi^{AJMTM_T}_{\alpha,M_\alpha}; n_\eta l_\eta, n_\nu l_\nu \Big\rangle \left\langle n_\eta l_\eta 00 l_\eta |\, 00 n_\eta l_\eta l_\eta \right\rangle_{\frac{a}{A-a}} . \end{aligned} \tag{A.12}$$

An algebraic expression for the general HO bracket can in this case be derived and it can be shown [24] to be

$$\left\langle nl00l |\, 00nll \right\rangle_{\frac{a}{A-a}} = (-1)^l \left( \frac{A-a}{A} \right)^{\frac{2n+l}{2}} . \tag{A.13}$$

## A.3 Overlap functions in a Hyperspherical Harmonics basis

The aim of this derivation is to make it possible to transform the expression for the overlap function in a radial HO basis, to a Hyperspherical Harmonic (HH) basis. This is the derivation used to compute the spectroscopic factors expanded in HH presented in Sec. 3.3.2.

# Definitions

The coordinates used are defined in the same way as in Chap. 3, which is a relative Jacobi coordinate system in T-configuration. The hyperspherical coordinates, the hyperradius, $\rho$, and hyperangle $\theta$ are defined by

$$\begin{aligned} \eta &= \rho\cos(\theta) \\ \nu &= \rho\sin(\theta), \end{aligned} \tag{A.14}$$

where $\theta \in [0, \pi/2]$. The volume element in this three-body problem is

$$d^3\eta d^3\nu = \eta^2 d\eta d\Omega_\eta \nu^2 d\nu d\Omega_\nu = \rho^5 \sin^2\theta\cos^2\theta d\rho d\theta d\Omega_\eta d\Omega_\nu.$$

The hyperspherical harmonics is defined as

$$\Gamma^{l_\eta l_\nu}_{KLM_L}(\Omega_5) = \Psi^{l_\eta l_\nu}_K(\theta)[Y_{l_\eta}(\hat{\eta})Y_{l_\nu}(\hat{\nu})]^{LM_L}, \tag{A.15}$$

where $Y_{l,m}(\hat{x})$ is the spherical harmonic, $\Omega_5 = \{\theta, \hat{\eta}, \hat{\nu}\}$ are the five hyperspherical polar angles and $K$ is the hypermomentum. $\Psi$ is the hyperangular function defined as

$$\Psi^{l_\eta,l_\nu}_K(\theta) \equiv N^{l_\nu,l_\eta}_K[\sin(\theta)]^{l_\nu}[\cos(\theta)]^{l_\eta} P_n^{l_\nu+\frac{1}{2},l_\eta+\frac{1}{2}}(\cos 2\theta), \tag{A.16}$$

where $N^{l_x,l_y}_K$ is a normalization factor and $P^{\alpha,\beta}_n(x)$ is the Jacobi polynomial. The hypermomentum is defined to be

$$K \equiv l_\eta + l_\nu + 2n \quad \text{where} \quad n = 0, 1, 2 \ldots.$$

The normalisation factor is

$$N^{l_\eta,l_\nu}_K \equiv \sqrt{\frac{2(n!)(K+2)(n+l_\nu+l_\eta+1)!}{\Gamma n + l_\nu + \frac{3}{2}\Gamma n + l_\eta + \frac{3}{2}}}.$$

In the case that the argument to the Jacobi Polynomial is real, which is true in this case, the Jacobi Polynomial can be expressed as

$$P_n^{\alpha,\beta}(x) \equiv \sum_s \binom{n+\alpha}{s}\binom{n+\beta}{n-s}\left(\frac{x-1}{2}\right)^{n-s}\left(\frac{x+1}{2}\right)^{s}, \tag{A.17}$$

for $x \in [-1,1]$.

The hyperangular function is a complete basis with the following normalization,

$$\int_0^{\pi/2} d\theta \sin^2(\theta)\cos^2(\theta)\Psi_K^{l_\eta,l_\nu}(\theta)\Psi_{K'}^{l_\eta,l_\nu}(\theta) = \delta_{K,K'}$$

To be consistent in notation we need to introduce a bra-ket notation and in that case we will define the hyperangular function as

$$\langle\theta|\ l_\eta, l_\nu, K\rangle \equiv \psi_K^{l_\eta,l_\nu}(\theta).$$

# Transformation to HH basis

The overlap function we are going to transform to a HH basis is defined in Eq. (3.13) and can be written as

$$u_{\alpha M_\alpha}^{A\lambda JM}(\vec{\eta},\vec{\nu}\,vec\chi) = \sum_{l_\eta l_\nu}\sum_{n_\eta n_\nu}^{N_{\max}} C_{\alpha,M_\alpha;n_\eta l_\eta n_\nu l_\nu}^{A\lambda JM} R_{n_\eta l_\eta}(\eta)R_{n_\nu l_\nu}(\nu)\Phi_{l_\eta l_\nu LS}^{JM}(\hat{\eta},\hat{\nu},\vec{\chi}), \tag{A.18}$$

where the factors in Eq. (3.13) are compactified into $C_{\alpha M_\alpha;n_\eta l_\eta n_\nu l_\nu}^{A\lambda JM}$, while $\vec{\chi}$ is the spin coordinate, and

$$\Phi_{l_\eta l_\nu LS}^{JM}(\hat{\eta},\hat{\nu},\vec{\chi}) = \left[[Y_{l_\eta}(\hat{\eta})Y_{l_\nu}(\hat{\nu})]^L\Phi^S\right]^{JM}.$$

To also be able to express the overlap function in a bra-ket notation we will define

$$\langle\eta,\nu|\ A\lambda JM;\alpha M_\alpha;(l_\eta l_\nu);N_{\max}\rangle \equiv \sum_{n_\eta n_\nu}^{N_{\max}} C_{n_\eta l_\eta n_\nu l_\nu}^{JMLS} R_{n_\eta l_\eta}(\eta)R_{n_\nu l_\nu}(\nu).$$

The aim is to express the overlap function in a HH basis, in this form:

$$u_{\alpha M_\alpha}^{A\lambda JM}(\rho,\theta,\hat{\eta},\hat{\nu},\vec{\chi}) = \frac{1}{\rho^{5/2}}\sum_K\sum_{l_\eta l_\nu}\chi_{\alpha M_\alpha K l_\eta l_\nu}^{A\lambda JM}\left[\Gamma_{K l_\eta l_\nu}^L(\Omega_5)\Phi^S\right]^{JM}, \tag{A.19}$$

where

$$\Gamma^{LM_L}_{Kl_\eta l_\nu}(\Omega_5) = \Psi^{l_\eta l_\nu}_K \left[Y_{l_\eta}(\hat{\eta})Y_{l_\nu}(\hat{\nu})\right]^{LM_L}$$

We can now start from Eq. (A.18) but using HH coordinates instead,

$$\begin{aligned} u^{A\lambda JM}_{\alpha M_\alpha}(\rho,\theta,\hat{\eta},\hat{\nu},\vec{\sigma}) &= \sum_{l_\eta l_\nu} \langle \rho,\theta|\ A\lambda JM;\alpha M_\alpha;(l_\eta l_\nu);N_{\max}\rangle\, \Phi^{JM}_{l_\eta l_\nu LS}(\hat{\eta},\hat{\nu},\vec{\sigma}) \\ &= \sum_K \sum_{l_\eta l_\nu} \langle \rho,\theta|\ Kl_\eta l_\nu\rangle \langle Kl_\eta l_\nu|\ A\lambda JM;\alpha M_\alpha;(l_\eta l_\nu);N_{\max}\rangle\, \Phi^{JM}_{l_\eta l_\nu LS}(\hat{\eta},\hat{\nu},\vec{\sigma}), \end{aligned} \tag{A.20}$$

where the last step was to insert a complete set of hyperangular basis functions and $\langle \rho,\theta|\ Kl_\eta l_\nu\rangle = \Psi_{Kl_\eta l_\nu}(\theta)\,\langle\rho|$. We can integrate over the hyperangle by inserting $\int d\theta' \sin^2\theta' \cos^2\theta'\, |\theta'\rangle\,\langle\theta'|$ in Eq. (A.20), which gives us

$$\begin{aligned} u^{A\lambda JM}_{\alpha M_\alpha}(\rho,\theta,\hat{\eta},\hat{\nu},\vec{\sigma}) &= \sum_{l_\eta l_\nu}\sum_K \left[\Gamma^L_{Kl_\eta l_\nu}\Phi^S\right]^{JM} \int d\theta' \sin^2\theta'\cos^2\theta' \\ &\quad \times \left\langle Kl_\eta l_\nu\right|\ \theta'\rangle \left\langle \rho,\theta'\right|\ A\lambda JM;\alpha M_\alpha;(l_\eta l_\nu);N_{\max}\big\rangle \\ &= \sum_{l_\eta l_\nu}\sum_K \left[\Gamma^L_{Kl_\eta l_\nu}\Phi^S\right]^{JM} \int d\theta' \sin^2\theta'\cos^2\theta' \\ &\quad \times \Psi^K_{l_\eta l_\nu}(\theta')^* \sum_{n_\eta n_\nu}^{N_{\max}} C^{A\lambda JM}_{\alpha M_\alpha;n_\eta l_\eta n_\nu l_\nu} R_{n_\eta l_\eta}(\rho,\theta') R_{n_\nu l_\nu}(\rho,\theta') \end{aligned} \tag{A.21}$$

By comparing Eq. (A.19) and (A.21) we can now identify $\chi^{LS;JM}_{Kl_\eta l_\nu}(\rho)$, which is the unknown function in the HH expansion. The hyperradial function in the HH expansion of the overlap function is

$$\chi^{A\lambda JM}_{\alpha M_\alpha,Kl_\eta l_\nu}(\rho) = \rho^{5/2} \int d\theta' \sin^2\theta'\cos^2\theta' \Psi^K_{l_\eta l_\nu}(\theta') \sum_{n_\eta n_\nu}^{N_{\max}} C^{A\lambda JM}_{\alpha M_\alpha;n_\eta l_\eta n_\nu l_\nu} R_{n_\eta l_\eta}(\eta) R_{n_\nu l_\nu}(\nu) \tag{A.22}$$

We are now in the position when we can compute the spectroscopic factor expanded in $K$. We can also compute the hyperradial function and study the radial behaviour for every HH component. This is used in the analysis presented in Chap. 3.

# Appendix B

# Transition Densities in a many-body basis

In this chapter the derivation of the transition densities calculated with ANICR is presented for the one-, and two-body case.

## B.1 One-body transition densities

The aim is to calculate the reduced one-body transition in a form containing matrix elements in the form $\left\langle A_f J_f M_f T_f M_{T,f} \right| a_k^\dagger a_l \left| A_i J_i M_i T_i M_{T,i} \right\rangle$, where $A$ is the number of nucleons, J (T) is the total spin (isospin), the quantum numbers $M$ ($M_T$) is the projection of the spin (isospin) and the initial (final) state is denoted by a subsript $i$ ($f$). The creation and annihilation operator creates and annihilates sp states $k$ and $l$, respectively. Matrix elements in this form are possible to obtain from wave functions in a SD basis computed in NCSM.

The Wigner-Eckart theorem gives

$$\left\langle A\lambda_f J_f M_f \right| [a_\alpha^\dagger \tilde{a}_\beta]_{J,M} \left| A\lambda_i J_i M_i \right\rangle = \hat{J}_f^{-1} (J_i M_i, JM | J_f M_f)(A\lambda_f J_f || [a_a^\dagger \tilde{a}_b]_J || A\lambda_i J_i) \tag{B.1}$$

where $\tilde{a}$ is an annihilation operator that behaves like a spherical tensor.The relation to the ordinary annihilation operator is: $\tilde{a}_\alpha = (-1)^{j_a + m_\alpha} a_{-\alpha}$ [6]. We are denoting single particle orbits (shells) with Roman letters and when also including the projection quantum numbers of the spin it is denoted

with Greek letters. So for example a possible set of single particle quantum numbers is $a = n_a, l_a, j_a$ and $\alpha = a, m_\alpha$. The last factor in Eq. B.1 is the reduced transition density that we finally want to compute.

We will start by projecting the left-hand side of Eq. (B.1) to an uncoupled basis,

$$\begin{aligned}
&\left\langle A\lambda_f J_f M_f \right| \left[a^\dagger_\alpha \tilde{a}_\beta\right]_{J,M} \left| A\lambda_i J_i M_i \right\rangle \\
&= \sum_{m_\alpha, m_\beta} (j_a m_\alpha, j_b m_\alpha | JM) \left\langle A\lambda_f J_f M_f \right| a^\dagger_\alpha \tilde{a}_\beta \left| A\lambda_i J_i M_i \right\rangle \\
&= \sum_{m_\alpha, m_\beta} (j_a m_\alpha, j_b m_\alpha | JM)(-1)^{j_b+m_\beta} \left\langle A\lambda_f J_f M_f \right| a^\dagger_\alpha a_{-\beta} \left| A\lambda_i J_i M_i \right\rangle \\
&= \sum_{m_\alpha, -m_\beta} (j_a m_\alpha, j_b - m_\alpha | JM)(-1)^{j_b-m_\beta} \left\langle A\lambda_f J_f M_f \right| a^\dagger_\alpha a_\beta \left| A\lambda_i J_i M_i \right\rangle .
\end{aligned} \tag{B.2}$$

We can now use the following relation[6],

$$(j_1 m_1, j_2 m_2 | j_3 m_3) = (-1)^{j_1 - m_1} \frac{\widehat{j_3}}{\widehat{j_2}} (j_3 m_3 j_1 - m_1 | j_2 m_2) \tag{B.3}$$

and apply it to Eq. (B.2).

$$\begin{aligned}
&\left\langle A\lambda_f J_f M_f \right| \left[a^\dagger_\alpha \tilde{a}_\beta\right]_{J,M} \left| A\lambda_i J_i M_i \right\rangle \\
&= \sum_{m_\alpha, m_\beta} (-1)^{j_b - m_\beta} (-1)^{-j_b + m_\beta} \frac{\widehat{J}}{\widehat{j_a}} (j_b m_\beta, JM | j_a m_\beta) \left\langle A\lambda_f J_f M_f \right| a^\dagger_\alpha a_\beta \left| A\lambda_i J_i M_i \right\rangle \\
&= \sum_{m_\alpha, m_\beta} \frac{\widehat{J}}{\widehat{j_a}} (j_b m_\beta, JM | j_a m_\beta) \left\langle A\lambda_f J_f M_f \right| a^\dagger_\alpha a_\beta \left| A\lambda_i J_i M_i \right\rangle
\end{aligned} \tag{B.4}$$

We are now in the position that we can insert Eq. (B.4) in Eq. (B.1) and write down the reduced transition density in an uncoupled basis,

$$\begin{aligned}
&(A\lambda_f J_f || [a^\dagger_a \tilde{a}_b]_J || A\lambda_i J_i) \\
&= \frac{\widehat{J}\widehat{J_f}}{(J_i M_i JM | J_f M_f)\widehat{j_a}} \sum_{m_\alpha, m_\beta} (j_b m_\beta, JM | j_a m_\alpha) \left\langle A\lambda_f J_f M_f \right| a^\dagger_\alpha a_\beta \left| A\lambda_i J_i M_i \right\rangle
\end{aligned} \tag{B.5}$$

By using the the relation between 3j symbols and Clebsch-Gordan coefficients, $(j_1 m_1, j_2 m_2 | j_3 m_3) = (-1)^{j_1 - j_2 + m_3} \widehat{j_3} \begin{pmatrix} j_1 & j_2 & j_3 \\ m_1 & m_2 & m_3 \end{pmatrix}$ we can express Eq. B.5 in terms of 3j symbols,

$$
\begin{aligned}
&(A\lambda_f J_f || [a_a^\dagger \tilde{a}_b]_J || A\lambda_i J_i) \\
&= \frac{\widehat{J}\widehat{J}_f}{(-1)^{J_i - J + M_f} \widehat{J}_f \begin{pmatrix} J_i & J & J_f \\ M_i & M & -M_f \end{pmatrix} \widehat{j}_a} \sum_{m_\alpha, m_\beta} (-1)^{j_b - J + m_\alpha} \widehat{j}_a \begin{pmatrix} j_b & J & j_a \\ m_b & M & -m_\alpha \end{pmatrix} \\
&\quad \times \left\langle A\lambda_f J_f M_f \middle| a_\alpha^\dagger a_\beta \middle| A\lambda_i J_i M_i \right\rangle \\
&= \frac{\widehat{J}(-1)^{-J_i - M_f}}{\begin{pmatrix} J_i & J & J_f \\ M_i & M & -M_f \end{pmatrix}} \sum_{m_\alpha, m_\beta} (-1)^{j_b + m_\alpha} \begin{pmatrix} j_b & J & j_a \\ m_b & M & -m_\alpha \end{pmatrix} \left\langle A\lambda_f J_f M_f \middle| a_\alpha^\dagger a_\beta \middle| A\lambda_i J_i M_i \right\rangle .
\end{aligned}
\tag{B.6}
$$

These uncoupled matrix elements states are possible to compute from many-body states in a SD basis.

## B.2 Two-body transition densities

The derivation of the two-body transition density will be done in a similar way to the one-body derivation. The main difference is that we need to do the uncoupling in two steps. First we need to project the expression to a uncoupled two-body basis and then uncouple the two-body states to single-body states, which we are able to compute. We need to take into account the normalization of the two-body state that needs to be normalized due to the Pauli principle, which is done with the normalization factor $N_{ab} = \frac{\sqrt{1 - \delta_{ab}(-1)^J}}{1 + \delta_{ab}}$ where $\delta_{ab} = 1$ if the two particles in the two-body state are of the same kind and in the same orbit.

We can in the same way as in eq. B.1 relate the transition density with a coupled matrix element by using the Wigner-Eckart theorem.

$$
\begin{aligned}
&\left\langle A\lambda_f J_f M_F \middle| \left[ [a_a^\dagger a_b^\dagger]_{J_{12}} [\tilde{a}_c \tilde{a}_d]_{J_{34}} \right]_{J,M} \middle| A\lambda_i J_i M_i \right\rangle \\
&\quad = J_f^{-1} (J_i M_i, JM | J_f M_d) (A\lambda_f J_f || \left[ [a_a^\dagger a_b^\dagger]_{J_{12}} [\tilde{a}_c \tilde{a}_d]_{J_{34}} \right]_J || A\lambda_i J_i)
\end{aligned}
\tag{B.7}
$$

We can now focus on the matrix element in Eq. B.7 and try to uncouple it to get an expression with uncoupled sp states, which we can compute.

$$
\begin{aligned}
&\left\langle A\lambda_f J_f M_F \right| \left[ [a_a^\dagger a_b^\dagger]_{J_{12}} [\tilde{a}_c \tilde{a}_d]_{J_{34}} \right]_{J,M} \left| A\lambda_i J_i M_i \right\rangle \\
&= \sum_{m_{12}, m_{34}} (j_{12} m_{12} j_{34} m_{34} | JM) \left\langle A\lambda_f J_f M_f \right| [a_a^\dagger a_b^\dagger]_{J_{12}} [\tilde{a}_c \tilde{a}_d]_{J_{34}} \left| A\lambda_i J_i M i \right\rangle \\
&= \sum_{m_\alpha, m_\beta} \sum_{\substack{m_{12}=m_\alpha+m_\beta \\ m_{34}=m_\delta+m_\gamma}} N_{ab}(J_{12})^{-1} N_{cd}(J_{34})^{-1} (j_a m_\alpha, j_b m_\beta | J_{12} M_{12}) (j_c m_\gamma j_d m_\delta | J_{34} M_{34}) \\
&\quad \times (J_{12} M_{12} J_{34} M_{34} | JM) \left\langle A\lambda_f J_f M_f \right| a_\alpha^\dagger a_\beta^\dagger \tilde{a}_\gamma \tilde{a}_\delta \left| A\lambda_i J_i M i \right\rangle \\
&= \sum_{m_\alpha, m_\beta} N_{ab}(J_{12})^{-1} N_{cd}(J_{34})^{-1} (j_a m_\alpha, j_b m_\beta | J_{12} M_{12}) (j_c m_\gamma j_d m_\delta | J_{34} M_{34}) \\
&\quad \times (J_{12} M_{12} J_{34} M_{34} | JM) (-1)^{j_c + m_\gamma} (-1)^{j_d + m_\delta} \left\langle A\lambda_f J_f M_f \right| a_\alpha^\dagger a_\beta^\dagger a_{-\gamma} a_{-\delta} \left| A\lambda_i J_i M i \right\rangle \\
&= \sum_{m_\alpha, m_\beta} (-1)^{j_c + j_d - m_\gamma - m_\delta} N_{ab}(J_{12})^{-1} N_{cd}(J_{34})^{-1} (j_a m_\alpha, j_b m_\beta | J_{12} M_{12}) \\
&\quad \times (j_c m_{-\gamma} j_d m_{-\delta} | J_{34} M_{34}) (J_{12} M_{12} J_{34} M_{34} | JM) \left\langle A\lambda_f J_f M_f \right| a_\alpha^\dagger a_\beta^\dagger a_\gamma a_\delta \left| A\lambda_i J_i M i \right\rangle = \\
&= \sum_{m_\alpha, m_\beta} (-1)^{j_c + j_d + M_{34}} N_{ab}(J_{12})^{-1} N_{cd}(J_{34})^{-1} (j_a m_\alpha, j_b m_\beta | J_{12} M_{12}) (-1)^{j_{34} - j_c - j_d} \\
&\quad \times (j_c m_\gamma j_d m_\delta | J_{34} - M_{34}) (J_{12} M_{12} J_{34} M_{34} | JM) \left\langle A\lambda_f J_f M_f \right| a_\alpha^\dagger a_\beta^\dagger a_\gamma a_\delta \left| A\lambda_i J_i M i \right\rangle \\
&= \sum_{m_\alpha, m_\beta} (-1)^{J_{34} - M_{34}} N_{ab}(J_{12})^{-1} N_{cd}(J_{34})^{-1} (j_a m_\alpha, j_b m_\beta | J_{12} M_{12}) \\
&\quad \times (j_c m_\gamma j_d m_\delta | J_{34} M_{34}) (J_{12} M_{12} J_{34} - M_{34} | JM) \left\langle A\lambda_f J_f M_f \right| a_\alpha^\dagger a_\beta^\dagger a_\gamma a_\delta \left| A\lambda_i J_i M i \right\rangle \\
&= \sum_{m_\alpha, m_\beta} (-1)^{J_{34} - M_{34}} N_{ab}(J_{12})^{-1} N_{cd}(J_{34})^{-1} (j_a m_\alpha, j_b m_\beta | J_{12} M_{12}) (j_c m_\gamma j_d m_\delta | J_{34} M_{34}) \\
&\quad \times (-1)^{M_{34} - J_{34}} \frac{\widehat{J}}{\widehat{J}_{12}} (J_{34} M_{34} JM | J_{12} M_{12}) \left\langle A\lambda_f J_f M_f \right| a_\alpha^\dagger a_\beta^\dagger a_\gamma a_\delta \left| A\lambda_i J_i M i \right\rangle \\
&= \sum_{m_\alpha, m_\beta} N_{ab}(J_{12})^{-1} N_{cd}(J_{34})^{-1} \frac{\widehat{J}}{\widehat{J}_{12}} (j_a m_\alpha, j_b m_\beta | J_{12} M_{12}) (j_c m_\gamma j_d m_\delta | J_{34} M_{34}) \\
&\quad \times (J_{34} M_{34} JM | J_{12} M_{12}) \left\langle A\lambda_f J_f M_f \right| a_\alpha^\dagger a_\beta^\dagger a_\gamma a_\delta \left| A\lambda_i J_i M i \right\rangle
\end{aligned}
$$

In the penultimate step we used Eq.(B.3). We can now write down the expression for the two-body transition density in a form that we are able to

compute.

$$
\begin{aligned}
&(A\lambda_f J_f||\left[[a_a^\dagger a_b^\dagger][\tilde{a}_c\tilde{a}_d]\right]_J||A\lambda_i J_i) \\
&\quad= \frac{\widehat{J}_f\widehat{J}}{(J_iM_iJM|J_fMf)}\sum_{\substack{m_\alpha,m_\beta,J_{12}\\ m_\delta,m_\gamma,J_{34}}} N_{ab}(J_{12})^{-1}N_{cd}(J_{34})^{-1}\frac{1}{\widehat{J}_{12}}(j_am_\alpha,j_bm_\beta|J_{12}M_{12}) \\
&\quad\times(j_cm_\gamma j_dm_\delta|J_{34}M_{34})(J_{34}M_{34}JM|J_{12}M_{12})\left\langle A\lambda_fJ_fM_f\right|a_\alpha^\dagger a_\beta^\dagger a_\gamma a_\delta\left|A\lambda_iJ_iMi\right\rangle = \\
&= \frac{\widehat{J}_f\widehat{J}}{(-1)^{J_i-J+M_f}\widehat{J}_f\begin{pmatrix}J_i & J & J_f\\ M_i & M & -M_f\end{pmatrix}}\sum_{\substack{m_\alpha,m_\beta,J_{12}\\ m_\delta,m_\gamma,J_{34}}} N_{ab}(J_{12})^{-1}N_{cd}(J_{34})^{-1}\frac{1}{\widehat{J}_{12}} \\
&\quad\times(-1)^{j_a-j_b+M_{12}}\widehat{J}_{12}\begin{pmatrix}j_a & j_b & J_{12}\\ m_\alpha & m_\beta & -M_{12}\end{pmatrix}(-1)^{j_c-j_d+M_{34}}\widehat{J}_{34}\begin{pmatrix}j_c & j_d & J_{34}\\ m_\alpha & m_\beta & -M_{34}\end{pmatrix} \\
&\quad\times(-1)^{J_{34}-J+M_{12}}\widehat{J}_{12}\begin{pmatrix}J_{34} & J & J_{12}\\ M_{34} & M & -M_{12}\end{pmatrix}\left\langle A\lambda_fJ_fM_f\right|a_\alpha^\dagger a_\beta^\dagger a_\gamma a_\delta\left|A\lambda_iJ_iMi\right\rangle \\
&= \frac{\widehat{J}}{(-1)^{J_i+M_f}\begin{pmatrix}J_i & J & J_f\\ M_i & M & -M_f\end{pmatrix}}\sum_{\substack{m_\alpha,m_\beta,J_{12}\\ m_\delta,m_\gamma,J_{34}}} N_{ab}(J_{12})^{-1}N_{cd}(J_{34})^{-1}\widehat{J}_{12}\widehat{J}_{34} \\
&\quad\times(-1)^{j_a-j_b+j_c-j_d+2M_{12}+J_{34}+M_{34}}\begin{pmatrix}j_a & j_b & J_{12}\\ m_\alpha & m_\beta & -M_{12}\end{pmatrix}\begin{pmatrix}j_c & j_d & J_{34}\\ m_\alpha & m_\beta & -M_{34}\end{pmatrix} \\
&\quad\times\begin{pmatrix}J_{34} & J & J_{12}\\ M_{34} & M & -M_{12}\end{pmatrix}\left\langle A\lambda_fJ_fM_f\right|a_\alpha^\dagger a_\beta^\dagger a_\gamma a_\delta\left|A\lambda_iJ_iMi\right\rangle
\end{aligned}
$$

# Bibliography


[1] P G Hansen and B Jonson. The Neutron Halo of Extremely Neutron-Rich Nuclei. *Europhys. Lett.*, 4(4), 1987.

[2] I Tanihata, H Hamagaki, O Hashimoto, Y Shida, N Yoshikawa, K Sugimoto, O Yamakawa, T Kobayashi, and N Takahashi. Measurements of Interaction Cross-Sections and Nuclear Radii in the Light P-Shell Region. *Phys. Rev. Lett.*, 55(24), 1985.

[3] MV Zhukov, BV Danilin, DV Fedorov, and JM Bang. Bound state properties of Borromean halo nuclei: $^{6}$He and $^{11}$Li. *Phys. Rep.*, 1993.

[4] Jane K. Cullum and Ralph A. Willoughby. *Lanczos Algorithms for Large Symmetric Eigenvalue Computations, Vol. 1.* Society for Industrial and Applied Mathematics, Philadelphia, PA, USA, 2002.

[5] Louis Komzsik. *The Lanczos Method: Evolution and Application.* Software, Environments and Tools. Society for Industrial and Applied Mathematics, 2003.

[6] Jouni Suhonen. *From nucleons to nucleus.* Springer, 2007.

[7] Willem H Dickhoff and Dimitri Van Neck. *Many-body Theory Exposed!: Propagator Description Of Quantum Mechanics In Many-body Systems.* World Scientific, Singapore, 2005.

[8] L Trlifaj. Simple formula for the general oscillator brackets. *Phys. Rev. C*, 5, 1972.

[9] D H Gloeckner and R D Lawson. Spurious center-of-mass motion. *Phys. Lett. B*, 53(4), 1974.

[10] R Machleidt and D R Entem. Chiral effective field theory and nuclear forces. *Phys. Rep.*, 503(1), 2011.

[11] A Ekström, G Baardsen, C Forssén, G Hagen, M Hjorth-Jensen, G R Jansen, R Machleidt, W Nazarewicz, T Papenbrock, J Sarich, and S M Wild. Optimized Chiral Nucleon-Nucleon Interaction at Next-to-Next-to-Leading Order. *Phys. Rev. Lett.*, 110(19), 2013.

[12] M Kortelainen, T Lesinski, J Moré, W Nazarewicz, J Sarich, N Schunck, M V Stoitsov, and S Wild. Nuclear energy density optimization. *Phys. Rev. C*, 82(2), 2010.

[13] S Bogner, R Furnstahl, and R Perry. Similarity renormalization group for nucleon-nucleon interactions. *Phys. Review. C*, 75(6), 2007.

[14] R J Furnstahl, G Hagen, and T Papenbrock. *Corrections to nuclear energies and radii in finite oscillator spaces*, volume 86. Phys. Rev. C, 2012.

[15] S N More, A Ekström, R J Furnstahl, G Hagen, and T Papenbrock. Universal properties of infrared oscillator basis extrapolations. *Physical Review C*, 87(4), 2013.

[16] S A Coon, M I Avetian, M K G Kruse, U van Kolck, P Maris, and J P Vary. Convergence properties of ab initio calculations of light nuclei in a harmonic oscillator basis. *Phys. Rev. C*, 86(5), 2012.

[17] M Brodeur, T Brunner, C Champagne, S Ettenauer, M Smith, A Lapierre, R Ringle, V Ryjkov, S Bacca, P Delheij, G Drake, D Lunney, A Schwenk, and J Dilling. First Direct Mass Measurement of the Two-Neutron Halo Nucleus $^{6}$He and Improved Mass for the Four-Neutron Halo $^{8}$He. *Phys. Rev. Lett.*, 108(5), 2012.

[18] S Bacca, N Barnea, and A Schwenk. Matter and charge radius of $^{6}$He in the hyperspherical-harmonics approach. *Phys. Rev. C*, 86(3), 2012.

[19] S Bacca, A Schwenk, G Hagen, and T Papenbrock. Helium halo nuclei from low-momentum interactions. *Eur. Phys. J. A*, 42(3), 2009.

[20] B D Carlsson and H T Johansson. Private communication. 2014.

[21] W. Nortershauser, T Neff, R. Sanchez, and I Sick. Charge radii and ground state structure of lithium isotopes: Experiment and theory re-examined. *Phys. Rev. C*, 84(2), 2011.

[22] A Ong, J C Berengut, and V V Flambaum. Effect of spin-orbit nuclear charge density corrections due to the anomalous magnetic moment on halo nuclei. *Phys. Rev. C*, 82(1), 2010.

[23] R J Furnstahl and A Schwenk. How should one formulate, extract and interpret 'non-observables' for nuclei? *J. Phys. G*, 37(6), 2010.

[24] P Navrátil. Cluster form factor calculation in the ab initio no-core shell model. *Phys. Rev. C*, 70(5), 2004.

[25] L Trlifaj. New relations for the general oscillator brackets. *Czech. J. Phys.*, 24(5), 1974.

[26] Petr Navrátil. Translationally invariant density. *Phys. Rev. C*, 70(1), 2004.

[27] I Brida and F M Nunes. Two-neutron overlap functions for $^6$He from a microscopic structure model. *Nuc. Phys. A*, 847(1-2), 2010.

[28] R Roth. Private communication. 2012.

[29] J M Bang, F G Gareev, W T Pinkston, and J S Vaagen. One-and two-nucleon overlap functions in nuclear physics. *Phys. Rep.*, 125(6), 1985.

[30] M Fabre de la Ripelle. The potential harmonic expansion method. *Annals of Physics*, 147(2), 1983.

[31] N Timofeyuk. Normalization of the (6He,4He) cross sections in the distorted-wave Born approximation. *Phys. Rev. C*, 63(5), 2001.

[32] Sofia Quaglioni, Carolina Romero-Redondo, and Petr Navrátil. Three-cluster dynamics within an ab initio framework. *Phys. Rev. C*, 88(3), 2013.

[33] G Papadimitriou, A T Kruppa, N Michel, W Nazarewicz, M Ploszajczak, and J Rotureau. Charge radii and neutron correlations in helium halo nuclei. *Phys. Rev. C*, 84(5), 2011.

[34] S C Pieper and R B Wiringa. Quantum Monte Carlo Calculations of Light Nuclei. *Annu. Rev. Nucl. Part. Sci.*, 51(nucl-th/0103005), 2001.

[35] H T Johansson. Private communication. 2014.

[36] Sofia Quaglioni and Petr Navrátil. Ab initio many-body calculations of n-3h, n-4he, p-3,4he, and n-10be scattering. *Phys. Rev. Lett.*, 101, 2008.

[37] Petr Navrátil, Sofia Quaglioni, Ionel Stetcu, and Bruce R Barrett. Recent developments in no-core shell-model calculations. *J. Phys. G*, 36(8), 2009.

[38] Y F Smirnov. Talmi transformations for particles with different masses. *Nuc. Phys.*, 27(2), 1961.